Bis(N-DABCO) magnesium(II) meso-arylporphyrin: Characterization, DFT calculations, catalytic degradation of rhodamine B dye and inhibiting activity of the COVID-19 virus and oxidase enzymes using molecular docking study

Taissir Fradi, Olfa Noureddine, Azhar Kechiche, Mohhieddine Guergueb, Florian Molton, Frédérique Loiseau, Thierry Roisnel, Ilona Turowska-Tyrk, Habib Nasri

Bis(*κN*-DABCO) Magnesium(II) *Meso*-arylporphyrin: Characterization, DFT Calculations, Catalytic Degradation of Rhodamine B Dye and Inhibiting Activity of the COVID-19 Virus and Oxidase enzymes using Molecular Docking Study

Taissir Fradi [a], Olfa Noureddine [b], Azhar Kechiche [a], Mohhieddine Guergueb [a], Florian Molton [c] , Frédérique Loiseau [c], Thierry Roisnel [d], Ilona Turowska-Tyrk [e], Habib Nasri [a,*]

[a] University of Monastir, Laboratory of Physical Chemistry of Material (LR01/ES/19), Monastir, Avenue de L 'environnement, 5019 Monastir, Tunisia.
[b] University of Monastir, Laboratory of Quantum and Statistical Physics (LR18ES18), Faculty of Sciences, Monastir, 5079, Tunisia
[c] Département de Chimie Moléculaire, Université Grenoble Alpes, 301 rue de la Chimie, CS 40700, Cedex 9, Grenoble 38058, France
[d] Institute of Chemical Sciences of Rennes, UMR 6226, University of Rennes 1, Beaulieu Campus, Rennes 35042, France.
[e] Faculty of Chemistry, Wroclaw University of Science and Technology, Wybrzete Wyspiańskiego 27, Wrocław 50-370, Poland.

Abstract

The present article describes the synthesis of the bis(1,4-diazabicyclo[2.2.2]octane))[*meso*-tetra(*para*-chlorophenyl)porphyrinato]magnesium(II) chloroform disolvate with the formula $[Mg(TClPP)(DABCO)_2]\cdot 2CHCl_3$ (**1**) and its characterization by ^1H NMR, IR, UV/Vis, fluorescence, and mass spectrometry as well as by cyclic voltammetry. The molecular structure of **1** was obtained by single crystal X-ray diffraction technique and the intermolecular interactions in the crystal lattice of **1** were investigated via Hirshfeld surfaces analysis. These electronic and structural properties of complex **1** are typical for pentacoordinated and hexacoordinated Mg(II) reported metalloporphyrins with *N*-donor axial ligands. The DFT studies on complex **1** were performed at the B3LYP/LANL2DZ levels of theory. The structural characteristics and global reactivity descriptors such as the chemical potential, global hardness, global softness, and the electrophilicity were investigated indicate that the title compound is very reactive and presents an important electron-accepting property.

Our new magnesium(II) metalloporphyrin species was tested to be a good inhibitor of two COVID-19 viruses and two oxidase enzymes using docking calculations. Furthermore, complex **1** exhibits encourageant catalytic degradation yield of the Rhodamine B dye.

* Corresponding author. Fax: +216 73 500 278.
E-mail address: hnasri1@gmail.com and habib.nasri@fsm.rnu.tn (Habib Nasri).

Keywords: Magnesium(II) porphyrin; UV-visible; X-ray molecular structure; Cyclic voltammetry; Catalytic degradation of the rhodamine B dye. DFT calculations

1. Introduction

Magnesium(II) porphyrin complexes have a wide range of applications in various fields, including (i) catalysis: these coordination compounds can act as catalysts in many reactions, such as oxidation, reduction, and isomerization reactions **[1-3]**, (ii) biomedical: these compounds have been studied for their potential use in treating various diseases, including cancer, cardiovascular disease, and neurodegenerative disorders **[4,5,6]**, (iii) materials science: Mg(II) metalloporphyrins have been incorporated into various materials, including polymers and thin films, for applications such as electronic devices and sensors **[7,8]**, (iv) energy: Mg(II) porphyrin species have been studied for their potential use in energy-related applications, such as solar cells and fuel cells **[9,10]** and (v) environmental: Magnesium(II) porphyrin complexes have been used in environmental applications such as water purification and air pollution control **[11,12]**. On the other hand, porphyrins and porphyrin-metal species are known to have antiviral and antibacterial properties. Recent studies have suggested that these compounds may have the potential to inhibit the activity of the COVID-19 virus **[13-16]**. It is interesting to note that among the 80 structures of mangnesium(II) metalloporphyrins reported in the Cambridge Structural Database (CSD Version 5.43, last update September 2022) **[17]**, 37 are pentacoordinated and 29 are hexacoordinated complexes. The pentacoordinated coordination compounds are of type $[Mg(Porph)(X)]^-$ (Porph = *meso*-arylporphyrin and X = anionic ligand) or [Mg(Porph)(L)] where L is a neutral *N*-donor or *O*-donor ligand while the hexacoordinate complexes are all type $[Mg(Porph)(L)_2]$ where L is a neutral *N*-donor or *O*-donor ligand. To predict and understand the penta- and hexa- coordination modes of Mg(II) porphyrin complexes is not so easy but it should depend, inter alia, on both the natures of the *meso*-arylporphyrin and the axial ligand. Back in 1976, Kadish *et al.,* **[18]** classified the following *meso*-arylporphyrins substituted in *para* positions of the phenyl groups by increasing electron donor effect (Figure 1) : $H_2T(CN)PP < H_2TFPP < H_2T(t\text{-}Bu)PP < H_2TClPP < H_2TPP < H_2T(OMe) = H_2TMPP) < H_2TBrPP < H_2TTP < H_2T(OH)PP$ where: $H_2T(CN)PP$

is the *meso*-tetra(*para*-cyanophenyl)porphyrin, H_2TFPP is the *meso*-tetra(*para*-fluorophenyl)porphyrin, H_2T(*t-Bu*)PP is the *meso*-tetra(*para*-tert-butylphenyl)porphyrin, the H_2TClPP is the *meso*-tetra(*para*-chlorophenyl)porphyrin, H_2TPP is the *meso*-tetraphenylporphyrin, the H_2T(OMe) = H_2TMPP is the *meso*-tetra(*para*-methoxyphenyl)porphyrin, the H_2TBrPP is the *meso*-tetra(*para*-bromophenyl)porphyrin, the H_2TTP is the *meso*-tetra(*para*-tolyl)porphyrin and H_2T(OH)PP is the *meso*-tetra(*para*-hydroxyphenyl)porphyrin.

If we take the example of the three aqua magnesium(II) complexes: Mg(TPP)(H_2O)] **[19]**, [Mg(TMPP)(H_2O)] **[20]** and [Mg(TBrPP)](H_2O)$_2$] **[21]** since the electron donor effect of the TPP, TMPP and TBrPP porphyrinates increases in the following order: TPP < TMPP < TBrPP, one can predict the increasing electronic density of the porphyrin core in the same order leading to the decrease of the electron deficiency of the Mg(II) center metal. Therefore, the probability of obtaining the di-aqua complex is higher than that of obtaining the mono-aqua. What we obtained is the opposite of what we expected because in solid state, we got the di-aqua with the TBrPP and the mono-aqua with the TPP and TMPP porphyrinates. With the 4-dimethylaminopyridine (DMAP) ligand in the solid state, with the TTP porphyrinate the bis-DMAP species exists with the formula [Mg(TTP)(DMAP)$_2$] **[22]** while with the TClPP porphyrinate the mono-DMAP [Mg(TClPP)(DMAP)] **[23]** complex is isolated. This is what is expected since the TTP porphyrinate is more electron donor than TClPP.

These examples of porphyrin complexes of Mg(II) with the aqua and DMAP ligands show that the use of the electron donor/withdrawing properties of a *meso*-arylporphyrins does not always explain the obtaining of a pentacoordinated or hexacoordinated Mg(II) metallo-*meso*-arylporphyrin complexes.

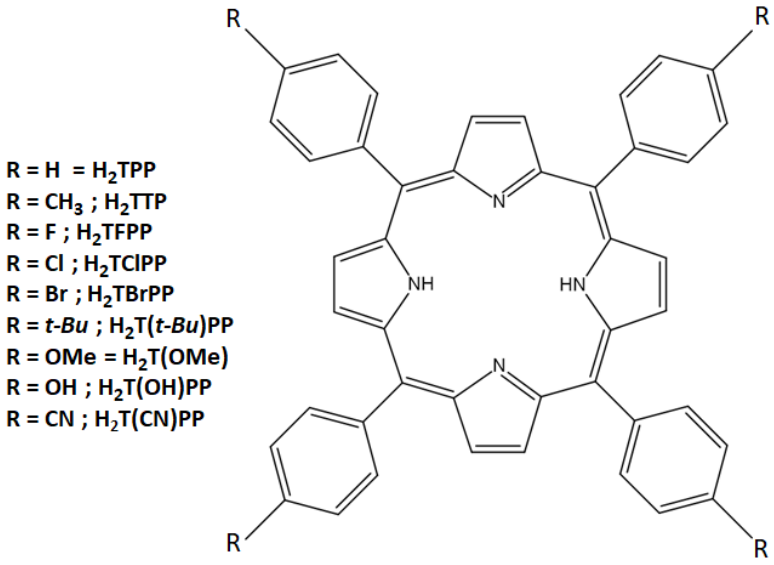

Figure 1. Schematic representation of some *meso*-arylporphyrins.

In this paper we report the preparation of a new hexacoordinated magnesium(II) porphyrin complex namely the bis(1,4-diazabicyclo[2.2.2]octane)[*meso*-tetra(*para*-chlorophenyl)porphyrinate]magnesium(II) chloroform disolvate with the formula $[Mg(TClPP)(DABCO)_2]\cdot 2CHCl_3$ (**1**). This new Mg(II) metaloporphyrin was characterized by UV/Vis, fluorescence, IR, ^{1}H NMR and mass spectrometry as well as by cyclic voltammetry. The molecular structure of **1** was determined by single crystal X-ray diffraction and the intermolecular interactions of **1** was studied by Hirshfeld surface analysis.

For further study of the electronic properties and chemical reactivity of complex **1**, theoretical calculations were performed. Complex **1** was tested as a catalyst in the degradation of the rhodamine B (RhB) dye by aqueous solution of hydrogen peroxide and by irradiation using blue light. In order to test the efficiency of complex **1** as inhibitor of the COVID-19 virus and oxidase enzymes, and to study how complex **1** species can anchor itself to the binding sites of these different receptors, docking calculations have been carried out with the iGEMDOCK program.

2. Experimental Section

2. 1. Materials and methods

The CHN elementary analysis results were made by the " *Institut National de Recherche et d'Analyse Physico-chimique du Technopole de Sidi Thabet (INRAP)*) ", Tunisia.

^{1}H NMR spectra were recorded at room temperature on a Bruker 300 Ultrashield spectrometer and chemical shifts are reported in ppm downfield from internal tetramethylsilane (TMS). Fourier-transformed IR spectra were recorded on a PerkinElmer Spectrum Two FT-IR spectrometer. UV/Vis spectra were recorded at room temperature under air using a WinASPECT PLUS (validation for SPECORD PLUS version 4.2) scanning spectrophotometer. Electrospray (ESI) mass spectrometry spectra were carried out using an amaZon speed ion trap instrument. Samples were ionized by electrospray ionization (ESI; capillary temperature = 320 °C, vaporizer temperature = 320°C, sheath gas flow rate = 5 mL/min).

The emission spectra were recorded at room temperature with a Horiba Scientific Fluoromax-4 Spectrofluorometer. The luminescence lifetime measurements were performed for excitation at λ= 450 nm using the second harmonic of a titanium–sapphire laser (picosecond Tsunami laser spectra physics 3950-M1BB and 39868- 03 pulse picker doubler) at an 800 kHz repetition rate. Fluotime 200 from AMS technologies was used for the decay acquisition. It consists of a GaAs microchannel plate photomultiplier tube (Hamamatsu model R3809U-50) followed by a time-correlated single photon counting system from Picoquant (PicoHarp300). The ultimate time resolution of the system is close to 30 ps. The luminescence decays were analyzed with the FLUOFIT software available from Picoquant. The mission quantum yields were determined at room temperature in dichloromethane solutions by using the optically dilute method **[24]**. [Zn(TPP)] in air-equilibrated dichloromethane solution was used as a quantum yield standard (ϕ_f = 0.031) **[25]**.

Cyclic voltammetry (CV) experiments were performed with a CH-660B potentiostat (CH Instruments). All analytical experiments were conducted at room temperature under an argon atmosphere (argon stream) in a standard one compartment, three-electrode electrochemical cell. Tetra-*n*-butylammonium perchlorate (TBAP) was used as a supporting electrolyte (0.2 M) in dichloromethane distilled over calcium hydride under argon. An automatic ohmic drop compensation procedure was systematically implemented before the CV data were recorded with electrolytic solutions containing the studied compounds at concentrations of ca. 10^{-3} M. CH Instruments vitreous carbon (φ = 3 mm) working electrodes were polished with 1 mm diamond paste before each recording. The $Ag/AgNO_3$ 0.01 M (TBAP 0.2 in CH_2Cl_2) redox couple was used as the reference electrode. The potential of the ferrocene/ferrocenium redox couple was used as an internal reference (86 mV vs. $Ag/AgNO_3$ under our experimental conditions). For comparison with previously published data, all potentials given in the text have been converted to values relative to the saturated calomel electrode (SCE) according to the following relationship: $E(SCE) = E(Ag/AgNO_3) + 298$ mV.

2.2. Synthetic methods

All reagents for the synthesis were used without any further purification. Solvents used in the spectroscopic and electrochemical measurements were of spectroscopic grade. The *meso*-tetra(*para*-chlorophenyl)porphyrin (H_2TClPP) and the [Mg(TClPP)] starting materials were prepared as described in the literature [26,27].

2.3. Synthesis of [Mg(TClPP)(DABCO)$_2$]·2CHCl$_3$ (1)

50 mg of the [Mg(TClPP)] starting material (0.064 mmol) and 100 mg of 1,4-diazabicyclo[2.2.2]octane (DABCO) (0.892 mmol) were dissolved in 10 mL of chloroform. The color of the starting solution changed from purple to green after four hours of reaction at room temperature. X-ray quality crystals of the title compound were obtained by slow diffusion of *n*-hexane through the chloroform solution after about one week (54 mg, 85 %).

Elemental analysis calcd (%) for $C_{58}H_{50}Cl_{10}MgN_8$ (Molecular weight = 1237.93), C 56.27, H 4.07, N 9.05; found: C 56.69, H 4.13, N 9.11; (ESI) (dichloromethane): *m*/*z* $[Mg(TClPP)(L)_2]^+$ (L = 1,4-diazabicyclo[2.2.2]octane $C_6H_{12}N_2$) calcd for $C_{56}H_{48}Cl_4MgN_8$: 999.15; found 992.06; UV–vis: λ_{max} (nm) in CH_2Cl_2: 430, 567, 606; FT-IR [solid neat, $\bar{\nu}$ (cm^{-1})]: [ν(CH) DABCO)] 3040, ν[(CH) Porph] 2970–3024, [ν(C=C) and [δ(CCH) Porph] 992; ^{1}H NMR (300 MHz, $CDCl_3$ δ (ppm): 8.81 (Hβ-pyrrol), 8.12-8.10 ($H_{o,o}$ Porph), 7.74 -7.72 ($H_{m,m'}$ Porph), 5.29 (H_L DABCO).

2.4. Quantum chemical calculations

All calculations (geometric parameters, electronic and vibrational properties) were performed by using Gaussian 09 program [28] and visualized in GaussView program [29].

2.5. X-ray structure determination

A purple prism shaped single crystal of dimensions 0.56 x 0.45 x 0.37 mm of complex **1** was chosen for an X-ray diffraction study. The data were collected at 150 K on a D8 VENTURE Bruker AXS CCDC diffractometer using Mo Kα radiation of wavelength 0.71073 Å. The data were corrected for absorption effects by using the SADABS program (Bruker AXS 2014) [30]. The structure was solved by the direct methods by using SIR-2019 program [31] and refined by full-matrix least-squares techniques on F^2 by using the SHELXL-2014 program [32]. The chlorine atom of one phenyl group of the TClPP porphyrinate is disordered in two positions (Cl1A and Cl1B) with refined position occupancies of 0.851 (6) and 0.149 (6), respectively. The atomic displacement parameters of the C29B,

Cl3B and Cl4B atoms are restrained to be equivalent and the C29B-Cl3B, C29B-Cl3B and C29B-Cl4B bond distances were restrained during the refinement using DFIX command [33]. All H atoms attached to C atoms were fixed geometrically and treated as riding with C—H = 0.93 Å (aromatic), 0.97 Å (methylene) and 0.98 Å (methine) with U_{iso}(H) = 1.2U_{eq}(C). A total of 840 parameters are refined with 5579 unique reflections and 4942 observed reflections [$F_o > 4\sigma(F_o)$]. The geometrical calculations were carried out using the program PLATON [34]. The molecular and packing diagrams were generated using the software MERCURY [35]. The crystallographic data and the structural refinement details for **I** are reported in Table 1. Selected bond lengths and angles for the compound are listed in Table 2.

Table 1. Crystal data and structural refinement for $[Mg(TClPP)(DABCO)_2]\cdot 2CHCl_3$ (**1**).

Formula	$C_{58}H_{50}Cl_{10}N_8Mg$
Crystal System	monoclinic
Crystal	*C2/n*
a (Å)	22.831(2)
b (Å)	12.463(1)
c (Å)	20.069(2)
β (°)	93.912(3)
V(Å^3)	5697.2(9)
Z	4
$\rho_{calc.}$/ g cm^{-3}	1.438
μ/ mm^{-1}	0.547
F(000)	2528
Crystal size (mm^3)	0.56 x 0.45 x 0.37
Crystal Color	purple
Crystal Shape	prism
T(K)	150 (2)
θ_{min} - θ_{max} (°)	2.193 – 25.999
Limiting indices	-28 ≤ h ≤ 28, -15 ≤ k ≤ 15, -24 ≤ l ≤ 20
R(int)	0.0247
Reflections collected/unique	26958 / 5579
Observed data [$I_o > 2\sigma(F_o)$]	4942
Parameters/Rest	840 / 3
S [Goodness of fit]	1.038
R_1[a], wR_2[c] [$F_o > 4\sigma(F_o)$]	R_1 = 0.0474, wR_2 = 0.1158
wR_2[b] [all data]	R_1 = 0.0533, wR_2 = 0.1204
Min./max. res. (eÅ^{-3})	0.542/ -0.789
CCDC	2236148

[a]: $R1 = \Sigma||F_o| - |F_c||/\Sigma|F_o|$, [b]: $wR2 = \{\Sigma[w(|F_o|^2 - |F_c|^2)^2]/\Sigma[w(|F_o|^2)^2]\}^{1/2}$.

Table 2. Selected bond lengths (Å) and angles (°) of (**1**).

	Magnesium coordination polyhedron		
Mg–N1	2.081(2)	N1-Mg-N2	89.83(6)
Mg–N2	2.065(2)	Mg–N4	2.474(2)
N1-Mg-N4	89.91(6)	N2-Mg-N4	90.75(6)
	DABCO Axial ligand		
N4–C24	1.477(3)	Mg-N4-C24	111.5(1)
N4-C28	1.471(3)	Mg-N4-C25	111.2(1)
N4-C25	1.477(3)	Mg-N4-C28	111.9(1)
C23-C24	1.552(4)	N4-C24-C23	111.1(2)
N3-C23	1.463(3)	N3-C23-C24	111.1(2)
N3-C26	1.457(3)	C23-N3-C26	107.7(2)
N3-C27	1.455(4)		

2.6. Oxidative degradation and photodegradation with H_2O_2

Oxidative degradation and photodegradation experiments of RhB dye were performed at room temperature in the absence and presence of light using 10 mg of the catalyst compound and 5 mL of an aqueous solution of RhB dye (at pH = 6, c = 25 mg/L) and H_2O_2 (10 mL/L). The dye – complex **1** molar ratio is 6.5. Stirring was maintained at 500 rpm. The resulting mixture was filtered, and then the concentration was recorded by measuring the absorbance at 554 nm for the RhB dye.

The decolonization yields (R%) are given by the following relationship (Equation 1):

$$\text{Yield } (\%) = (A_0 - A_t / A_0) * 100 \qquad \textbf{(Eq. 1)}$$

where A_0 is the initial Absorption of dyes and A_t is the Absorption at different time intervals.

3. Results and Discussion

3.1. Synthesis of $[Mg(TClPP)(DABCO)_2]\cdot 2CHCl_3$ (1)

The reaction of the [*meso*-tetra(*para*-chlorophenyl)porphyrinato]magnesium(II) ([Mg(TClPP)]) starting material with an excess of 1,4-diazabicyclo[2.2.2]octane (DABCO) in chloroform at room temperature yields the bis(κN-DABCO)[*meso*-tetra(*para*-chlorophenyl)porphyrinato]magnesium(II)

chloroform disolvate with the formula $[Mg(TClPP)(DABCO)_2]\cdot 2CHCl_3$ (**1**) as given by the X-ray molecular structure (Scheme 1). We obtained, as expected, the bis-*N*-donor-DABCO $[Mg(TClPP)(DABCO)_2]\cdot 2CHCl_3$ complex, and not the mono-*N*-donor- κN-DABCO magnesium(II) TClPP coordination complex [Mg(TClPP)(DABCO)] since the TClPP porphyrinate presents a quite good electron withdrawing character. This electronically depletes the center metal Mg(II) and therefore increases the probability for accepting more electrons by Mg^{2+}. On the other hand, in a previous work, we reported the preparation and the characterization of the bis-κN-DABCO-Mg(II) $[Mg(TPBP)(DABCO)_2]$ species [36] where TPBP is the *meso*-tetrakis[4(benzoyloxy)phenyl]porphinate which also presents a good withdrawing character.

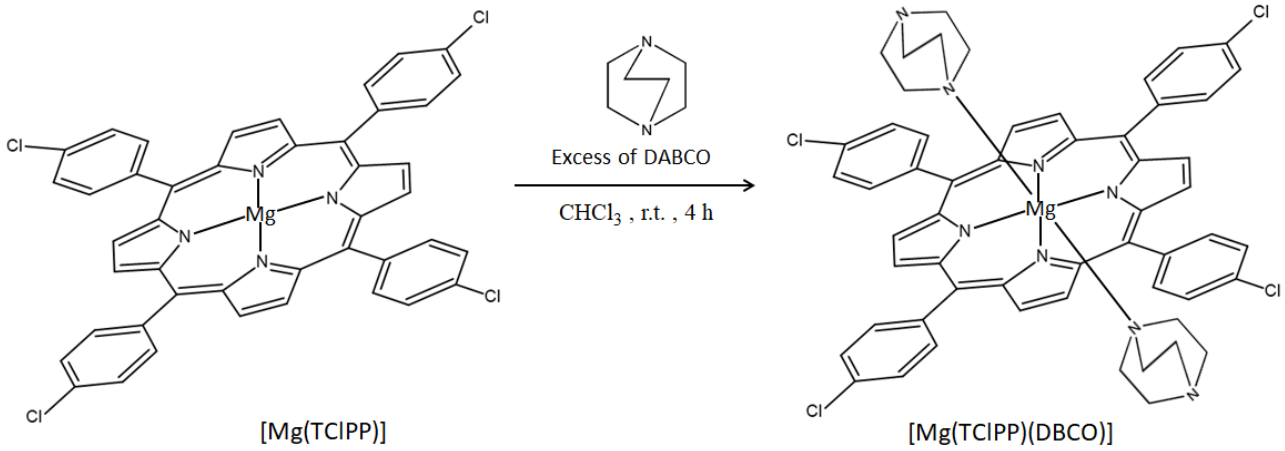

Scheme 1. Scheme of the preparation of $[Mg(TClPP)(DABCO)_2]\cdot 2CHCl_3$ (**1**)

3.2. Mass spectrometry data of complex 1

Electrospray ionization (ESI) mass spectroscopy experiment on **1** was performed in positive and negative ion modes where several peaks have been characterized (Figure 2, Table S1). The presence of the $[Mg(TClPP)+3H]^{3+}$ and $[Mg(TClPP)(DABCO)+2H]^{2+}$ fragments in the MS ESI (+ and -) is an indication of the presence of the bis(κN-DABCO)-Mg(II)-TClPP (**1**) derivative in solution.

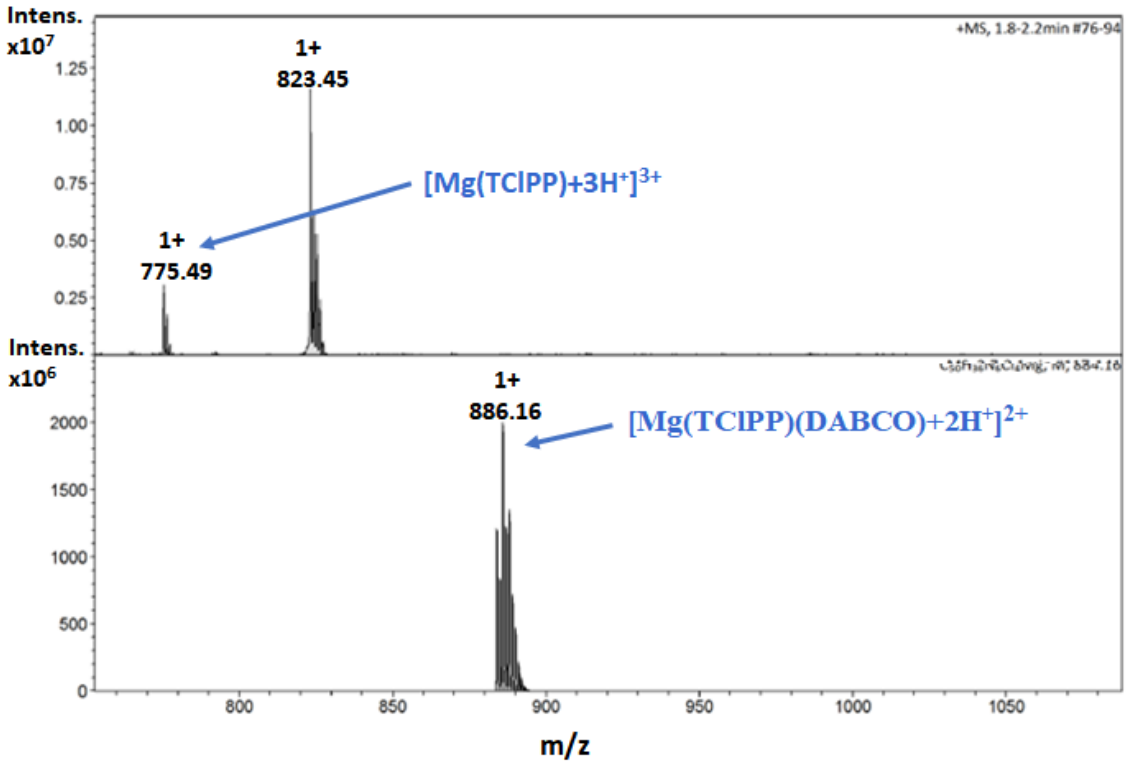

Figure 2. Electrospray mass spectrometry (ESI+ spectra of complex **1**. The spectra were recorded in dichloromethane with a concentration of 5.10^{-3} M.

3.3. Proton NMR and IR spectroscopy

The ^{1}H NMR spectrum of **1** is depicted in Figure 3. The β-pyrrolic protons (H_{β}) and the $H_{o,o'}$, $H_{m,m'}$ protons of the *meso*-phenyl rings of the TClPP moiety resonate at 8.81, 8.12/8.10 and 7.74/7.72 ppm, respectively. The values of these chemical shifts are very close to those of the corresponding free base porphyrin H_2TClPP indicating the diamagnetic character for complex **1**. The protons of the -CH_2-N- groups of the two DABCO axial ligands resonate at 5.29 ppm which are low field shifted compared to those of the non-coordinated DABCO molecule which resonate at 2.46 ppm. This could be explained by the withdrawing effect of the chlorine atoms at the *para* positions of the phenyl groups of the TClPP moiety leading to the decrease of the electronic density of the DABCO ligands and therefore increasing the chemical shift of these protons.

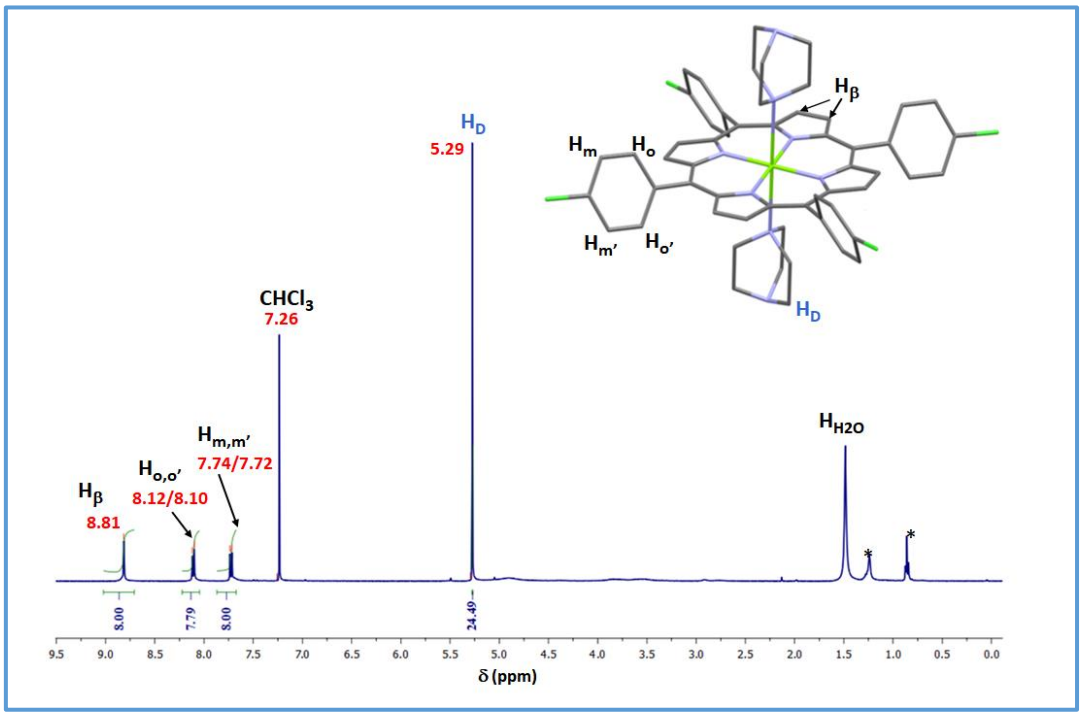

Figure 3. ^{1}H NMR spectrum of [Mg(TClPP)(DABCO)$_2$]·2CHCl$_3$ (**1**) recorded in CDCl$_3$ at room temperature with concentration C ~10^{-3} M.

Figure 4 illustrates the IR spectrum of complex **1**. The weak absorption band a 3040 cm^{-1} is attributed to the ν(CH) stretching vibration of the DABCO axial ligand. This value of ν(CH) is very close to that attributed to the DABCO axial ligand coordinated to the magnesium(II) and cobalt(II) porphyrin complexes [Mg(TPBP)(DABCO)$_2$] (TPBP = *meso*-tetrakis[*para*-(benzoyloxy)phenyl]porphyrinate) **[36]** and [Co^{II}(TPBP)(DABCO)$_2$] **[37]** with values of 3032 and 3030 cm^{-1}, respectively.

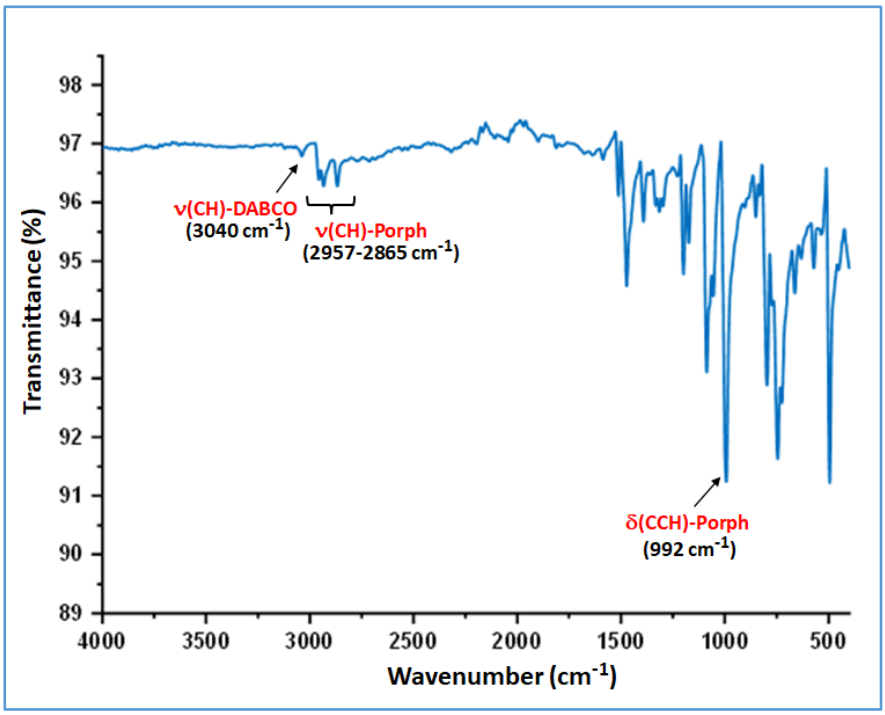

Figure 4. Neat IR spectrum of complex **1**.

3.4. Photophysical properties of complex 1

The absorption spectrum of complex **1** (Figure 5) consists of a strong Soret band ($S_o \leftarrow S_2$ transition) centered at 430 nm and two weaker absorption bands known as Q bands ($S_o \leftarrow S_1$ transition): Q(0,1) (567 nm) and Q(0,0) (607 nm). These absorption values of $[Mg(TClPP)(DABCO)_2]\cdot 2CHCl_3$ (**1**) are very close to those of the related Mg(II) *meso*-arylmetalloporphyrins (Table S2), e.g., for the [Mg(TClPP)(DMAP)] (DMAP = 4-dimethylaminopyridine) **[23]** the λ_{max} values of the Soret and the O(1,0) et Q(0,0) are 432, 570 and 609 nm, respectively.

An inspection of Table S2 shows that the Soret band value of the tetracoordinated, pentacoordinated and hexacoordinated magnesium(II) *meso*-arylporphyrin complexes range between 424 and 435 nm, the Q(1,0) band value of these species are in the range [563 – 576] nm while the Q(0,0) band value of all three types of Mg(II) *meso*-arylporphyrins is between 608 and 620 nm. This indicates that the UV/Vis spectroscopy technique is not able to differentiate between a tetra-, penta- and hexacoordinated Mg(II) *meso*-arylporphyrin coordination compounds in solution.

The emission spectrum of complex **1** is illustrated along with its absorption spectrum in Figure 5. The later spectrum corresponds to the $S_o \leftarrow S_1$ transition where the Q(1,0) and Q(0,0) emission bands are

centered at 609 nm and 664 nm, respectively. These values are very close to those of the [Mg(TClPP)(DMAP)] and [Mg(TTP)(4-pypo)$_2$] (TTP = *meso*-tetratolylporphyrinate, 4-pypo = 4-pyrrolidinopyridine) **[23,38]** related species with λ_{max} values of 612/611 and 666/663 nm of the Q(1,0) and Q(0,0), respectively. This indicates that the photophysical properties of Mg(II) metalloporphyrins didn't depend on the nature of the *meso*-arylporphyrin or the nature of the *N*-donor neutral axial ligand (Table S2).

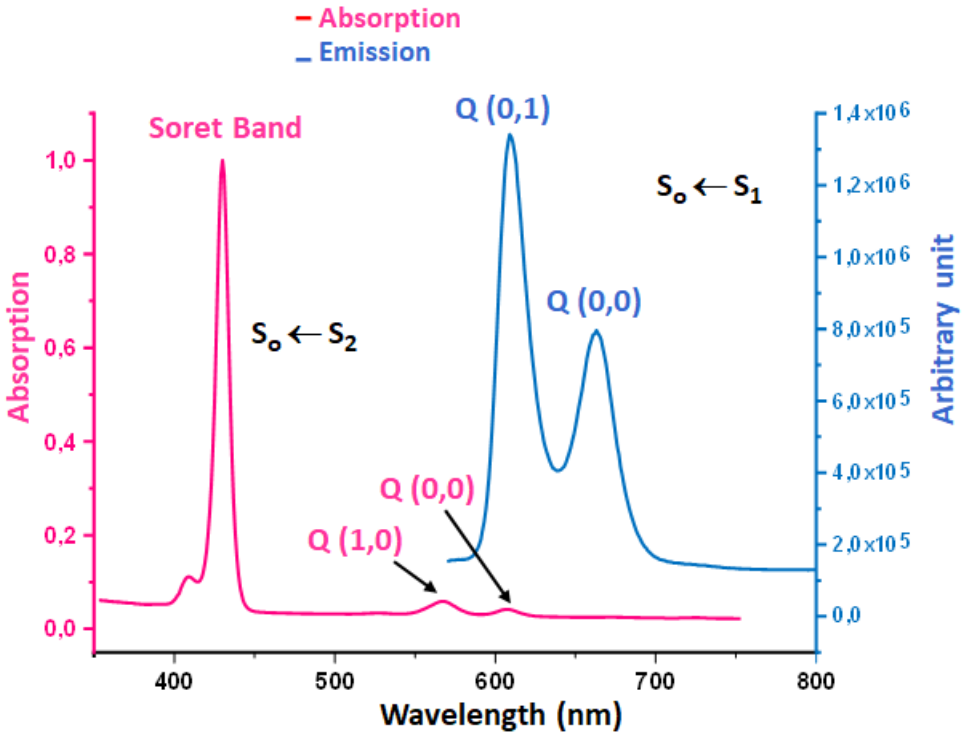

Figure 5. UV/Vis spectrum (red color) and fluorescence spectrum (blue color) of complex **1**. Spectra recorded in dichloromethane with concentrations ~ 10^{-6} M.

The optical gap energy ($E_{g\text{-}opt}$) of **1** was determined from the $(\alpha h\nu)^2$ versus the photon energy ($E = h\nu$) **[39]** where α is absorption coefficient, h is the Planck constant and *ν* is the frequency ($\nu = 1/\lambda$) (Figure S1). The value of $E_{g\text{-}opt}$ of complex **1** is 1.995 eV which is normal for *meso*-arylporphyrins and metalloporphyrins and is indicative of a semi-conductor character of [Mg(TClPP)(DABCO)$_2$]·2CHCl$_3$ (**1**).

3.5. X-ray Structures of [Mg(TClPP)(DABCO)$_2$]·2CHCl$_3$ (1)

The asymmetric unit of **1** contains one half [Mg(TClPP)(DABCO)$_2$] complex and one disorder chloroform solvent molecule. The space group is *C2/c* with four formula units by cell leading to the formula [Mg(TClPP)(DABCO)$_2$]·2CHCl$_3$ for **1** (Figure S2). A selection of distances and angles of complex **1** is given in Table 2 while Figure 6 depicts an Ortep view of [Mg(TClPP)(DABCO)$_2$].

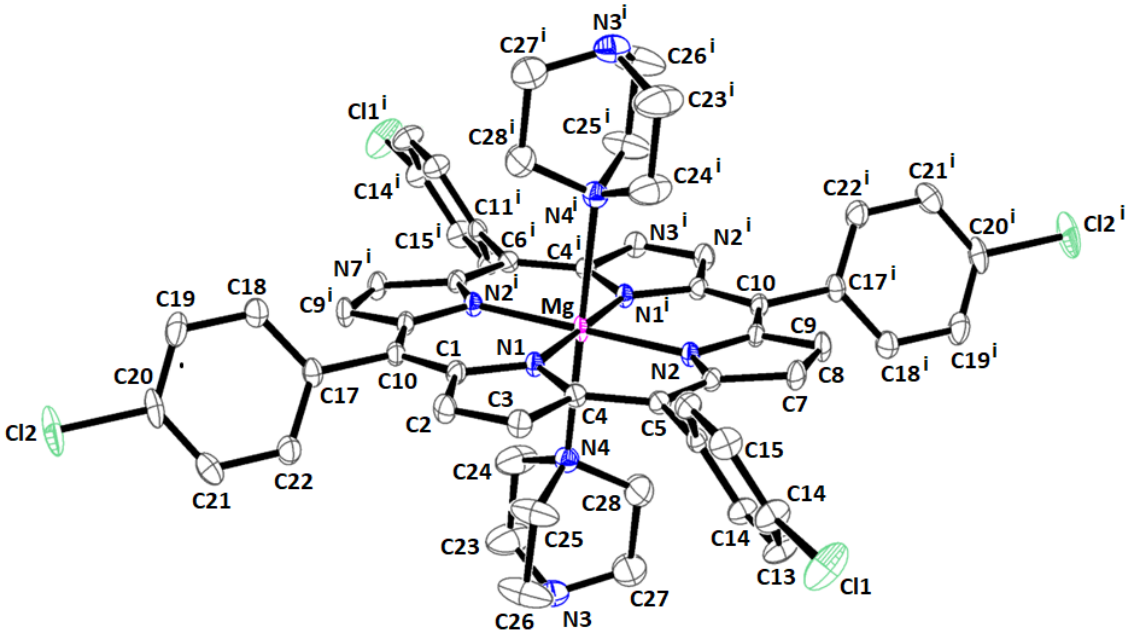

Figure 6. ORTEP drawing of [Mg(TClPP)(DABCO)$_2$] with thermal ellipsoids drawn at 50% probability. The hydrogen atoms are removed for clarity and only the major position of the disordered chlorine atom Cl1A of the porphyrin is shown.

The average equatorial distance between the magnesium(II) central ion and the nitrogen atoms of the porphyrin ring (Mg—N$_p$) of complex **1** is 2.0733(15) which is quite higher than those of the two Mg(II) related metalloporphyrins [Mg(TPBP)(DABCO)$_2$] (TPBP = *meso*- tetrakis[4-(benzoyloxy)phenyl]porphinate) **[36]** and [Mg(Porph1)(μ$_2$-DABCO)(Porph2)Zn] (Porph1 = 4-(2-(diphenylphosphino)ethylthio)phenyl)-10,20-bis(mesityl)porphyrinate, Porph2 = 4-(2-(diphenylphosphino)ethoxy)phenyl)-10,20-bis(mesityl)porphyrinate) **[50]** with values of 2.066 and 2.061 Å, respectively. Nevertheless, the Mg—N$_p$ bond length of **1** is in the range [2.061 – 2.074] Å of hexacoordinated magnesium(II) metalloporphyrins but quite smaller than those of the pentacoordinated Mg(II) porphyrin complexes which are in the range [2.082(3) – 2.1197(16)] Å (Table 3). The

Mg—N(DABCO) distance value of 2.4741(17) Å for complex **1** is very close to that of the [Mg(TPBP)(DABCO)$_2$] related complex which is 2.487 Å indicating that the nature of the *meso*-arylporphyrin has no effect on la geometry of the [Mg(Porph)(DABCO)$_2$] species.

Table 3. Selected bond lengths [Å] and angles [°] for [Mg(TClPP)(DABCO)$_2$]·2CHCl$_3$ (**1**) and several related Mg(II) porphyrin complexes.

Complex	Mg—N$_p$ [a]	M—X$_L$ [c]	Mg—P$_C$ [c]	Ref.
	Pentacoodinated Magnesium(II) Metalloporphyrins			
[Mg(TTP)(DMAP)$_2$]·2CH$_2$Cl$_2$	2,0703(14)	2.3165(14)/ 2.3166(14)	0.00	**[22]**
[Mg(TBrPP)(HIm)] [d]	2.094 (2)	2.120 (3)	0.52	**[44]**
[Mg(TPP)(H$_2$O)] [e]	2.092 (7)	2.012 (6)	0.460	**[19]**
[Mg(TMPP)(H$_2$O)] [f]	2.087	2.075	0.440	**[20]**
[Mg(TClPP)(DMAP)]·1/2C$_6$H$_{14}$	2.082 (3)	2.130 (4)	0.3709 (14)	**[23]**
[Bu$_4$N][Mg(TPP)(HCO$_3$)] [e]	2.101 (3)	1.959(2)	0.478	**[51]**
[K(222)][Mg(TPP)(N$_3$)] [g,e]	2.1187 (16)	1.997 (2)	0.6629 (7)	**[36]**
	Hexacoordinated Magnesium(II) Metalloporphyrins			
[Mg(TPBP)(DABCO)$_2$] [h]	2.066	2.487	0.000	**[36]**
[Mg(Porph1)(μ$_2$-DABCO)(Porph2)Zn] [i,j]	2.061	2.329	0.000	**[50]**
[Mg(TClPP)(DABCO)$_2$]·2CHCl$_3$ (**1**)	2.0733(15)	2.4741(17)	0.000	t.w.
[Mg(TPP)(HMTA)$_2$] [e]	2.067(5)	2.473(2)	0.000	**[49]**
[Mg(TPP)(1-MeIm)$_2$] [e]	2.079	2.297	0.000	**[52]**
[Mg(TPP)(pipz)$_2$] [e]	2.073	2.423	0.000	**[52]**
[Mg(TPP)(py)$_2$] [e]	2.072	2.376	0.000	**[53]**
[Mg(TBrPP)(H$_2$O)$_2$] [d]	2.069	2.221	0.000	**[21]**
[Mg(TPBP)(HTMA)$_2$] [k]	2.074	2.439	0.000	**[36]**
[Mg(TPP)(4-Picoline-N)$_2$] [e]	2.070	2.385	0.000	**[52]**
{[Mg(TPBP)(4,4'-bpy)$_2$]}$_n$ [k]	2.066	2.320	0.000	**[47]**
[Mg(TTP)(DMAP)$_2$] [l]	2.0703(14)	2.317(2)	0.000	**[22]**
	DABCO-Mg(II) non-porphyrinic complexes			
[Mg{Me)$_2$(THF)}$_2$(μ$_2$-DABCO)] -		2.208/3.083	-	**[60]**
[Mg(μ$_2$-H)(μ$_2$-(N{Si(CH$_3$)$_2$}(μ$_2$-DABCO)]$_2$		2.148/1.993	-	**[55]**

[a]: Mg—Np = average equatorial M–Npyrrole bond length, [b]: Mg—X$_L$ = distance between Mg atom and the nitrogen atom of axial ligand, [c]: Mg—P$_C$ = distance between Mg and the mean plane made by the 24-atom core of the porphyrin (P$_C$), [d]: TBrPP = *meso*-tetra(*para*-bromophenyl)porphyrinate, [e]: TPP = *meso*-

tetraphenylporphyrinate, [f]: TMPP = *meso*-tetra(*para*-methoxyphenyl)porphyrinate, [g]: 222 = cryptand-222, [h]: TPBP = *meso*-tetrakis[4(benzoyloxy)phenyl]porphinate, [i]: Porph1 = 4-(2-(diphenylphosphino)ethylthio) phenyl)-10,20-bis(mesityl)porphyrinate, [j]: Porph2 = 4-(2-(diphenylphosphino)ethoxy)phenyl)-10,20-bis(mesityl)porphyrinate, l: TTP = *meso*-tetra(*para*-tolyl)porphyrinate.

In the crystal packing of complex **1**, the [Mg(TClPP)(DABCO)$_2$] molecules form 1D chains parallel to the [001] direction (Figure 7). These [Mg(TClPP)(DABCO)$_2$] molecules and the chloroform solvent molecules are weakly bonded by C—H···Cl non-conventional hydrogen bonds (Table S3).

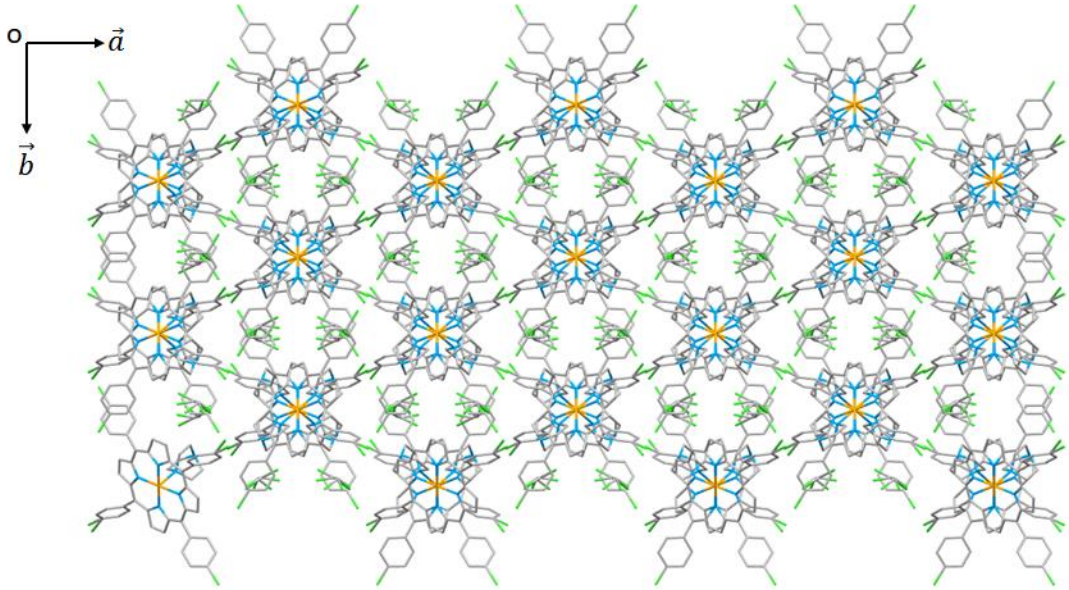

Figure 7. Projection of the crystal lattice of **1** down the c axis.

3.6. Hirshfeld Surface Analysis

The Crystal Explorer 17.5 program **[56]** was used to generate the Hirshfeld Surface (HS) and 2D fingerprint plots of complex **1**. The normalized contact distance, d_{norm}, based on the d_e, d_i (from the HS to the nearest atom outside-inside and inside-internal the surface, respectively) and the van der Waals radii of the atom (r^{vdW}) is given by the following equation :

$$d_{norm} = \frac{d_i - r_i^{vdW}}{r_i^{vdW}} + \frac{d_e - r_e^{vdW}}{r_e^{vdW}} \qquad \textbf{(Eq. 2)}$$

The d_{norm} HS shows all the contacts of the crystal structure. The blue and white regions of the HS indicate that the contacts are longer and closer to the van der Waals of the involved atoms, while the red regions indicate the shorter contacts than the sum of the van der Waas radii (Figure 8). The intermolecular interactions C—H···Cl present practically the same distance values that those obtained using the PLATON program (see the X-ray molecular structure section) The overall two-dimensional fingerprint plot for complex **1** are illustrated in Figure S3 and the percentage contributions from the different interatomic contacts to the Hirshfeld surfaces are as follows: H…Cl (33.8%), H…H (33.5%), H…C (10.3%) and H…N (1.8%).

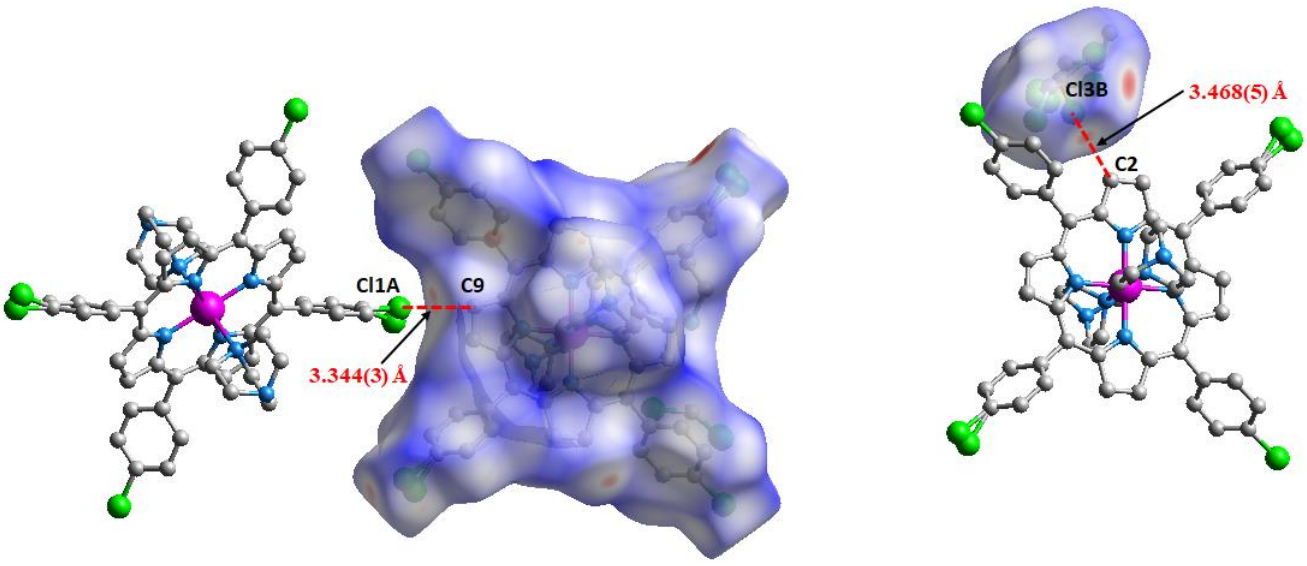

Figure 8. Hirshfeld surfaces of complex **1** mapped over d_{norm}.

The sharp index mapped on HS of complex **1** is depicted in Figure 9-a showing the absence of blue and red triangles indicates that there are no π···π stacking interactions in the crystal structure of **1**. The curvedness plots did not exhibit flat surface patches indicating the absence of planar stacking (Figure 8-b).

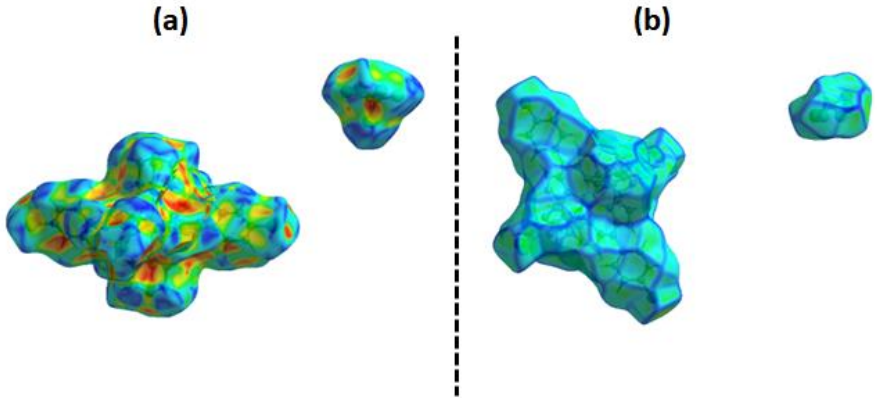

Figure 9. **(a):** Shape index surfaces of complex **1**, **(b):** Curvedness surfaces of complex **1**.

3.7. Cyclic voltammetry

The cyclic voltammogram of **1** is depicted in Figure 10. In the anodic part of this voltammogram are shown three one-electron reversible oxidation waves (O1/R1, O2/R2 and O3/R3) attributed to the oxidation of the porphyrin core of complex **1** (Scheme 2). One reversible reduction wave attributed to the oxidation of the porphyrin macrocycle is observed in the negative part of the voltammogram of [Mg(TClPP)(DABCO)$_2$]·2CHCl$_3$ (**1**) (R4/O4, Scheme 2).

$[Mg^{II}(TPP)(DABCO)_2]$	$-e^-$	⟷	$[Mg^{II}(TPP)^+(DABCO)_2]^+$	(O1/R1)
$[Mg^{II}(TPP)^+(DABCO)_2]^+$	$-e^-$	⟷	$[Mg^{II}(TPP)^{2+}(DABCO)_2]^{2+}$	(O2/R2)
$[Mg^{II}(TPP)^{2+}(DABCO)_2]^{2+}$	$-e^-$	⟷	$[Mg^{II}(TPP)^{3+}(DABCO)_2]^{3+}$	(O3/R3)
$[Mg^{II}(TPP)(DABCO)_2]$	$+e^-$	⟷	$[Mg^{II}(TPP)^-(DABCO)_2]^-$	(R4/O5)

Scheme 2. Redox equations involving the reductions and the oxidations waves of complex **1**.

The half potential values of these four waves are 0.71, 0.96, 1.21 and -1.54 V for O1/R1, O2/R2; O3/R3 and R4/O4, respectively which are very close to those of the related pentacoordinated and hexacoordinated Mg(II) *meso*-arylporphyrins, e.g., for [Mg(TTP)(4-pypo)$_2$] and [Mg(TClPP)(DMAP)] **[38,23]** the $E_{1/2}$ values of the reversible waves O1/R1, O2/R2; O3/R3 and R4/O4 are 0.62/0.63, 1.04/0.91, 1.26/1.22 and -1.60/-1.42 V, respectively. As a conclusion of the cyclic voltammetry investigation on complex **1** we notice that magnesium(II) *meso*-arylporphyrin coordination compounds exhibit very close electrochemical properties whatever the type of the functional group present in the *para*-positions of the phenyls of the *meso*-porphyrin and whatever the nature of the axial *N*-donor ligand(s).

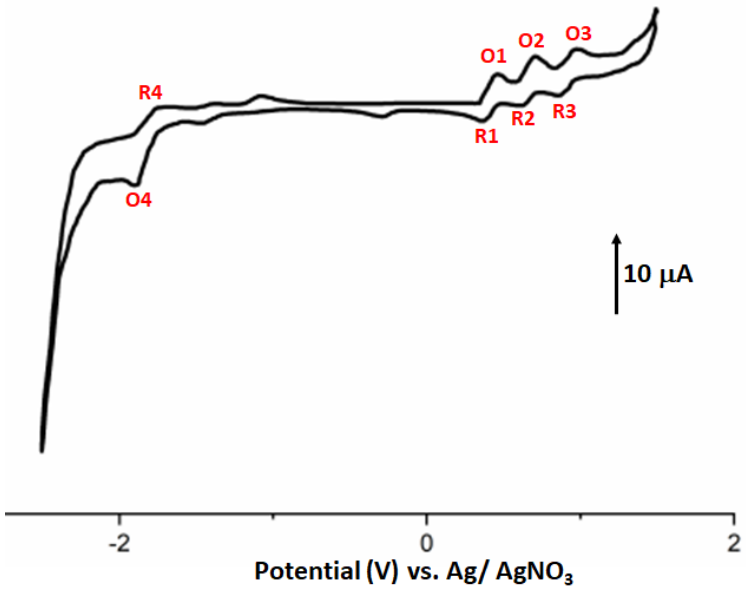

Figure 10. Cyclic voltammogram of complex **1**. The solvent used is CH_2Cl_2, and the concentration is ca. 10^{-3} M in 0.2 M TBAP, 50 mV/s, vitreous carbon working electrode (Ø = 3 mm).

3.8. Computational calculations

3.8.1. The optimized molecular structure

The optimized molecular structure of $[Mg(TClPP)(DABCO)_2]\cdot 2CHCl_3$ (**1**) is depicted in Figure 11 determined by using the density functional theory (DFT) at the B3LYP/LANL2DZ method.

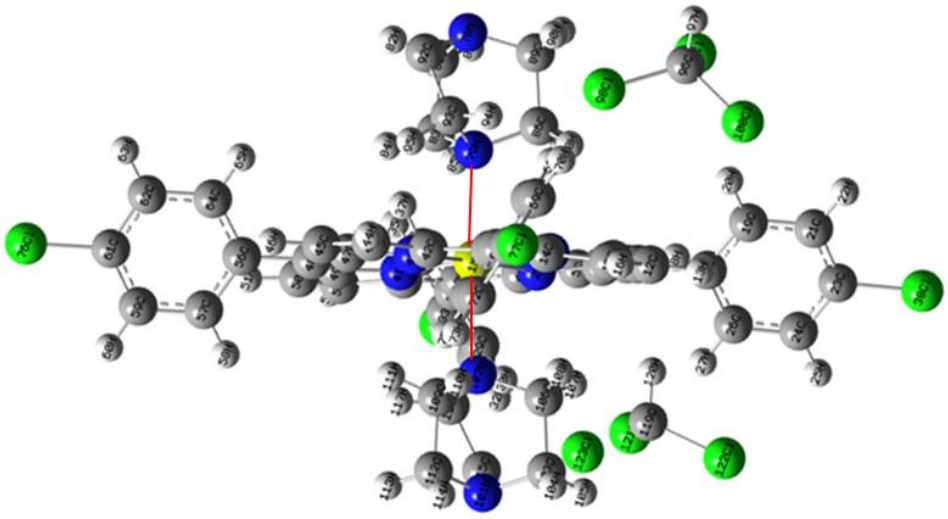

Figure 11. Optimized molecular structure of $[Mg(TClPP)(DABCO)_2]$ (**1**) using DFT/ B3LYP/LANL2DZ method in gas phase.

In Table S4 are given the experimental and the theoretical bond distances and angle values of complex **1**. As shown in this table, the calculated geometry parameters of **1** are close to those given by the X-ray molecular structure. Thus, the experimental bond distances Mg-N1, Mg-N2 and Mg-N4 are 2.0812(15), 2.0653(15) and 2.4741(17 Å, respectively while the theoretical distance values are 2.052/2.085, 2.052/2.100, and 2.330 Å, respectively. These slight differences between experimental and theoretical distances in complex **1** are attributed to the fact that the theoretical values were obtained considering a single isolated molecule in the gaseous phase.

3.8.2. Molecular electrostatic potential (MEP)

Molecular electrostatic potential (MEP) surface of $[Mg(TClPP)(DABCO)_2]\cdot 2CHCl_3$ (**1**) was calculated and plotted by the Gaussview 05 program. It is used to observe the charge distributions of different species **[57-59]**. This surface makes it possible to predict the behavior and reactivity of molecular systems. It is related to the electron density, which recognizes electrophilic and nucleophilic sites, as well as hydrogen-type interactions. Figure 12 shows the MEP map of the complex **1**. As clearly seen, the negative potential regions are represented by red color and the major positive potential regions are shown in blue.

We used the DFT/B3LYP/LanL2DZ process to determine the MEP contour maps of the electrostatic potential of **1**. The color code used to indicate the potential increase is in the order : red < orange < yellow < blue. The blue color refers to the potential positive values while the red color refers to the potential negative values. This color code was used to obtain the MEP maps by mapping electrostatic potential to the total electron density (Figure 12). In this figure, the color code of the maps is between $-1.2.10^{-2}$ u.a. (red color) and $1.2.10^{-2}$ u.a. (blue color). The electrophilic reactivity of a molecule indicates the strongest attraction is represented in blue in the MEP map while nucleophilic reactivity of a given molecule indicates the strongest repulsion of electrons, is shown in red color in a MEP map. The green color of a MEP map is indicative of zero potential. Two MEP maps of complex **1** are shown in Figure 12 indicating that the accepting strength (blue color) is important around the Mg(II) center metal and the DABCO axial ligands. This leads us to conclude that a nucleophilic substitution of the DABCO ligand is possible.

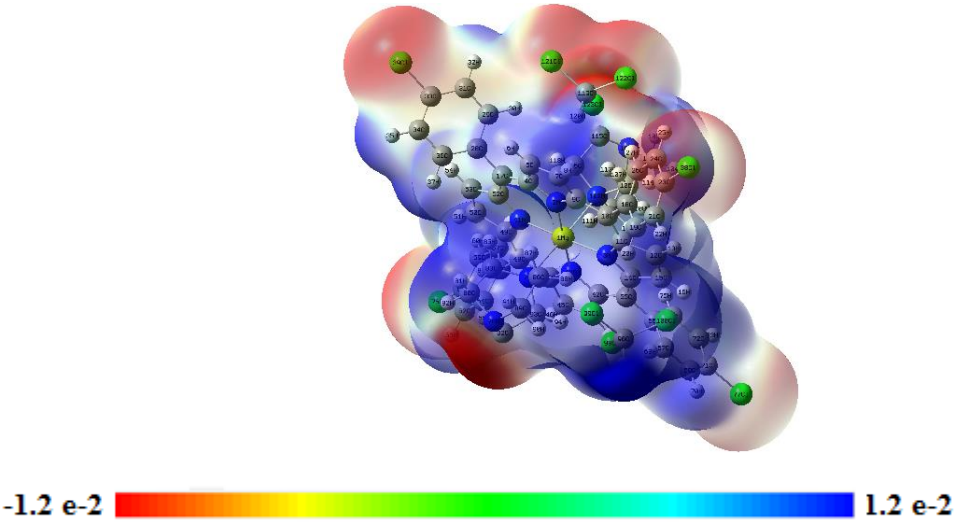

Figure 12. Calculated electrostatic potential surface of complex **1**.

3.8.3. Frontier molecular orbitals (FMOs): HOMO and LUMO analysis

The lowest unoccupied molecular orbital (LUMO) and the highest occupied molecular orbital (HOMO) are the most important orbitals in a molecule. They are very useful to understand the chemical stability of the molecule **[60,59]**. The 3D plots of the HOMO, HOMO-1, LUMO and LUMO+1 frontier orbitals of [Mg(TClPP)(DABCO)$_2$]·2CHCl$_3$ (**1**) are given in Figure 13 and Figure S4, respectively.

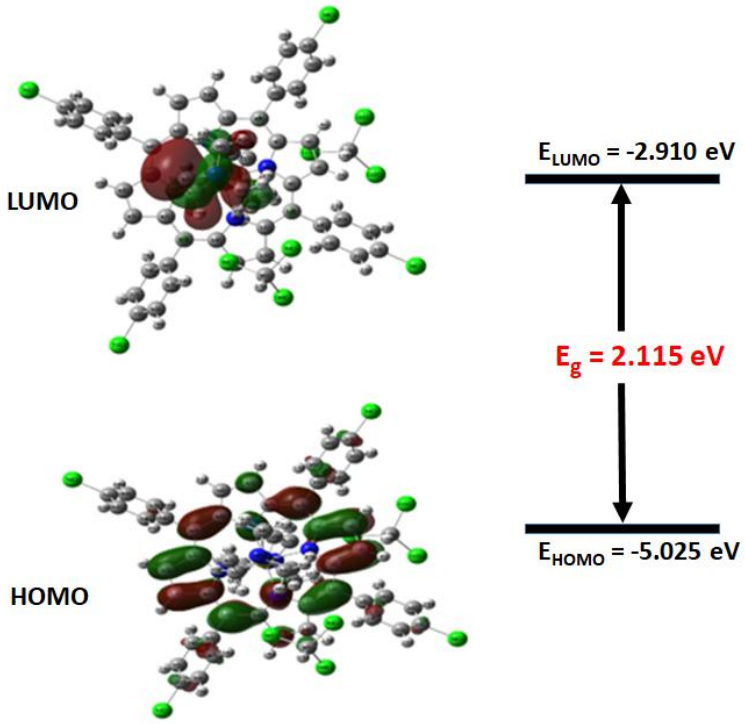

Figure 13. The HOMO and LUMO frontier molecular orbitals of complex **1**.

The HOMO-LUMO Gap energy (E_g) values were calculated in gas phase by TD-DFT/B3LYP/ LANL2DZ level. As shown in Figure 13**,** the negative phase is presented in green color and the positive phase is illustrated in red. The calculation results reveal that the energy difference E_{HOMO}-E_{LUMO} (E_g) is equal to 2.155 eV while the calculated E_{HOMO-1} - E_{LUMO+1} energy is 2.392 eV.

The capacity of complex **1** to donate or accept electrons is given by the global reactive parameters (Table 4). These parameters are also used to confirm the stability and the chemical reactivity of studied molecules. The calculated electrophilic index ψ value is 7.444 eV indicating that complex **1** is a good acceptor of electrons better than that of the related species [Mg(TClPP)(DMAP)] **[23]** with a value of 5.553 eV. The chemical hardness (η) value of 1 is 1.057 eV which is slightly smaller than that of the [Mg(TClPP)(DMAP)] complex (η = 1.300 eV) indicates that complex **1** is not very hard while the softness value is 0.473 $(eV)^{-1}$. The high negative value of the chemical potential (μ = -3.967 eV) which testifies to the high stability of $[Mg(TClPP)(DABCO)_2]\cdot 2CHCl_3$ (**1**). All these parameters' values let us suppose that complex **1** is stable, quite soft and reactive. In this connection, and to test the reactivity of complex 1, we studied the degradation activity of this coordination compound on the Rhodamine B dye (see section 3.9).

Table 4. TD-DFT calculations of complex **1**, $[Mg(TTP)(DMAP)_2]$ **[22]** and [Mg(TClPP)(DMAP)] **[23]** at the B3LYP/LanL2DZ level of theory (gas phase) of HOMO-LUMO energy gap, chemical potential, electronegativity, global hardness, global softness, and electrophilicity index.

Function	Values		
	Complex **1**	$[Mg(TTP)(DMAP)_2]$* **[22]**	[Mg(TClPP)(DMAP)]** **[23]**
E_{HOMO} (eV)	-5.024	-4.108	-5.101
E_{LUMO} (eV)	-2.910	-1.555	-2.500
E_{LUMO}-E_{HOMO} = *Gap energy* (eV)[a]	2.115	2.553	2.601
Ionisation potential (eV)[b]	5.024	4.108	5.101
Electron affinity (eV)[c]	-2.910	-1.555	-2.500
Chemical potential μ (eV)[d]	-3.967	-3.831	-3.800
Mulliken electronegativity χ [e]	3.967	2.831	3.800
Global hardness η (eV)	1.057	-	1.300
Softness S $(eV)^{-1}$	0.473	-	0.384
Global electrophilicity index ψ (eV)[i]	7.444	-	5.553

*: in dichloromethane solvent, **: in gas phase.

[a]: *Gap energy* = E_{LUMO}-E_{HOMO}, [b]: *Ionisation potential* ≈ -E_{HOMO}, [c]: *Electron affinity* ≈ -E_{LUMO}, [d]: *Chemical potential* $\mu = 1/2(E_{LUMO} + E_{LUMO})$, [e]: *Mulliken electronegativity* = $\chi = -\mu$, [f]: *Global hardness* $\eta = 1/2(E_{LUMO} - E_{LUMO})$, [g]: *Global Softness* $S = 1/2\eta$, [i]: *Global electrophilicity index* $\psi = \mu^2/2\eta$.

3.8.4. Molecular docking analysis

3.8.4.1. Computational details

Molecular docking calculations of proteins (PDB codes: 1HD2, 1H4O, ACE2 and ORF8) with $[Mg(TClPP)(DABCO)_2]\cdot 2CHCl_3$ (**1**) complex was carried out using the iGEMDOCK program [61]. This program is based on a generic evolutionary method (GA) and an empirical scoring function, the setting of which is the following: the size of the population is 800, the number of generations is 80 and the number of solutions is equal to 10. The 3D structures of the different proteins were extracted from the RCSB PDB database of the Structural Bioinformatics Research Laboratory (http://www.rcsb.org) [62]. Both proteins (receptors) and the ligand (complex **1**) were adapted with Discovery Studio Visualizer software [63].

3.8.4.2. Docking calculations

A molecular docking investigation was carried out on complex **1** to test the efficiency of this porphyrinic complex as inhibitor of the COVID-19 virus and several oxidase enzymes using docking calculations known to be a powerful theoretical method for studying molecular interactions [23,64,65]. This is how it is possible to determine the orientation of molecules (inhibitors) associated with their targeted proteins (receptors) in order to calculate their energy scores.

3.8.4.3. Docking results of complex 1 with ACE2 and ORF8 proteins

Molecular docking calculations were carried out with two structures of SARS-COV-2 protein. The first protein is the Angiotensin-Converting enzyme 2 "ACE2" (PDB code: 1H4O). The second is the Open Reading Frame 8 "ORF8" protein (PDB code: 7F5F). The structures of the target proteins were adapted with Discover Studio Visualizer software. Moreover, all crystallographic water molecules were removed. While docking calculations, we have determined ten poses but we presented only the best ones, which correspond to the minimal energies. Bond energies, such as van der Waals, hydrogen bond and electrostatic interaction that occurred between complex **1** and proteins were identified (as shown in Table 5). Binding energy informs us on the strength compound binds to the pocket of a protein. We have also plotted in Figure 14 the different interactions of $[Mg(TClPP)(DABCO)_2]\cdot 2CHCl_3$ (**1**) (ligand) in the active sites of 1HD2 protein and in Figure S5, 1H4O protein. Evidently, the ligand is linked to the receptor by several interactions such as alkyl, π-alkyl, π-anion, π-donor, conventional hydrogen bonding, carbon-hydrogen bond, etc. The examination of Table 5 revealed that the ACE2-$MgTClPP(DABCO)_2$ system possesses the strongest energy score which is equal to -125.15 kcal/mol. Note that this energy is the sum of the three energy interactions: hydrogen bond, vdW and electronic interactions. As well, it has the strongest van der Waals interaction with a value of -122.82 kcal/mol. Thereafter, the ORF8-

MgTClPP(DABCO)$_2$ system exhibits a total energy score equal to -101.15 kcal/mol with an important van der Waals interaction (E_{VDW}= -101.15 kcal/mol). For the same Angiotensin-Converting enzyme 2 SARS-COV-2 protein, complex **1** presents much better inhibition than using the triorganotin(IV) carboxylate complex R_3SnL (R = C4H9, L = the 2-chlorophenyl ethanoate) **[66]**.

It can be concluded that complex **1** is a good inhibitor of the coronavirus and can therefore be effective in controlling this disease.

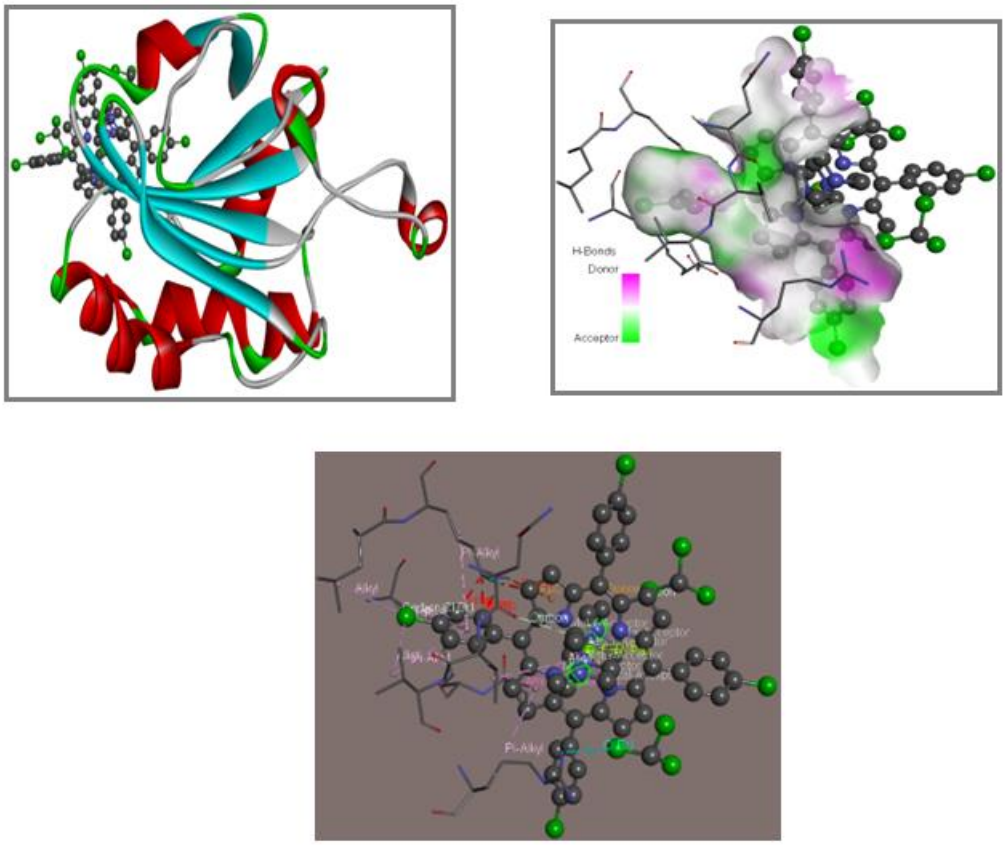

Figure 14**.** Docking interactions of complex **1** in the active sites of 1HD2 protein.

3.8.4.4. Docking study on complex 1 with Human peroxidase enzyme and PRDX5

In this part, we explore the molecular docking calculations on complex **1** that is predicted to be relevant for antioxidant activity. Calculations were carried out against two oxidase enzymes: Human Peroxidase enzyme (PDB code1HD2) (Figure 15) and Peroxiredoxin 5 (PRDX5) (PDB code1H4O) (Figure S6).

The " Human Peroxidase-[Mg(TClPP)(DABCO)$_2$]·2$CHCl_3$ " system presents the highest total energy value of -89.68 kcal/mol with an important van der Waals interaction (-89.68 kcal/mol). For the

peroxiredoxin 5 (PRDX5) protein, results show that complex **1** has bonded effectively with the target sites of the receptor with total energy equal to -72.80 and EVDW = -72.80 kcal/mol (as illustrated in Table 5).

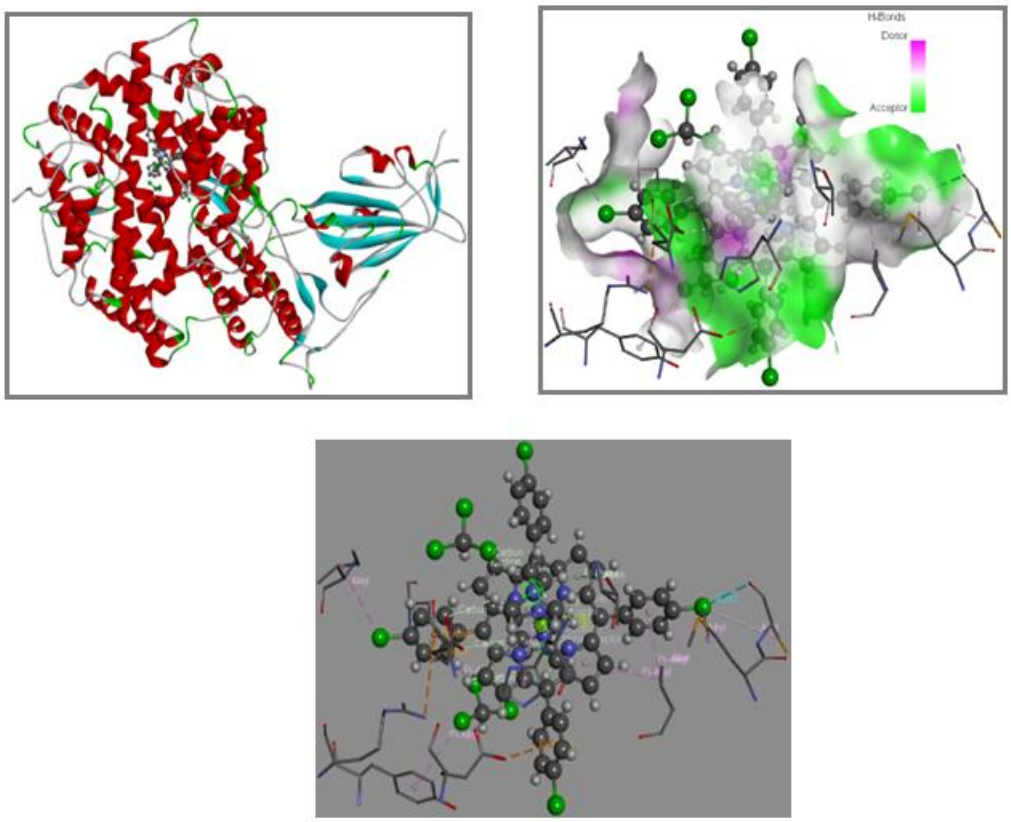

Figure 15**.** Orientation of complex **1** in the active sites of ACE2 and (d) ORF8 receptor.

Table 5. Docking score energies of complex **1** with Human Peroxidase, Peroxiredoxin 5, Angiotensin-Converting and Open Reading Frame 8 receptors.

Ligand	$[Mg(TClPP)(DABCO)_2]\cdot 2CHCl_3$ (**1**)			
	Oxidase enzymes		SARS-COV-2	
Target protein	Human Peroxidase enzyme	Peroxiredoxin 5 (PRDX5)	Angiotensin-Converting enzyme 2 (ACE2)	Open Reading Frame 8 (ORF8)
	PDB code1HD2	PDB code1H4O	PDB code 7UON	PDB code 7F5F
Total energy	-89.68	-72.80	-125.15	-101.15
Van der Waal	-89.68	-72.80	-122.82	-101.15
H-bond	0	0	-2.33	0
Electronic	0	0	0	0

3.9. Oxidative degradation of Rhodamine B dye using complex 1

3.9.1. Degradation using an aqueous solution of H_2O_2 using complex 1

It is noteworthy that synthetic dyes constitute a large part of water pollutants due to the sewage discharge containing such very harmful and even carcinogenic chemical species. This is why for more than three decades a very important number of investigations concerning the degradation of these toxic species were performed [67-70]. According to IUPAC nomenclature, rhodamine B (RhB) is called N-[9-(ortho-carboxyphenyl)-6-(diethylamino)-3H-xanthen-3-yli-dene] diethyl ammonium chloride. It exhibits maximum absorbance at a wavelength of 554 nm [71]. This dye is very toxic and according to Gao *et al.,* [72] it has also been associated with the disruption of central nervous systems and other vital organs, including the liver, brain and kidney. Several methods have been reported concerning the degradation of the RhB dye [73,74]. In order to get more insights into the degradation procedures to RhB dye, we investigated the use of our Magnesium(II) bis(DABCO) porphyrin complex (**1**) in the degradation of the RhB dye.

The UV/vis spectroscopy was employed to investigate the oxidative degradation of the rhodamine B (RhB) dye using aqueous solution of hydrogen peroxide as the oxidant in the presence of complex **1** as catalyst. In Figure 16 represents the absorption of the RhB dye in the absence (Reference = blank) and presence of H_2O_2 for several degradation times. The degradation of RhB was monitored by following the variation of λ_{max} of the absorption band of the RhB species at ~ 554 nm (in aqueous solution at room temperature).

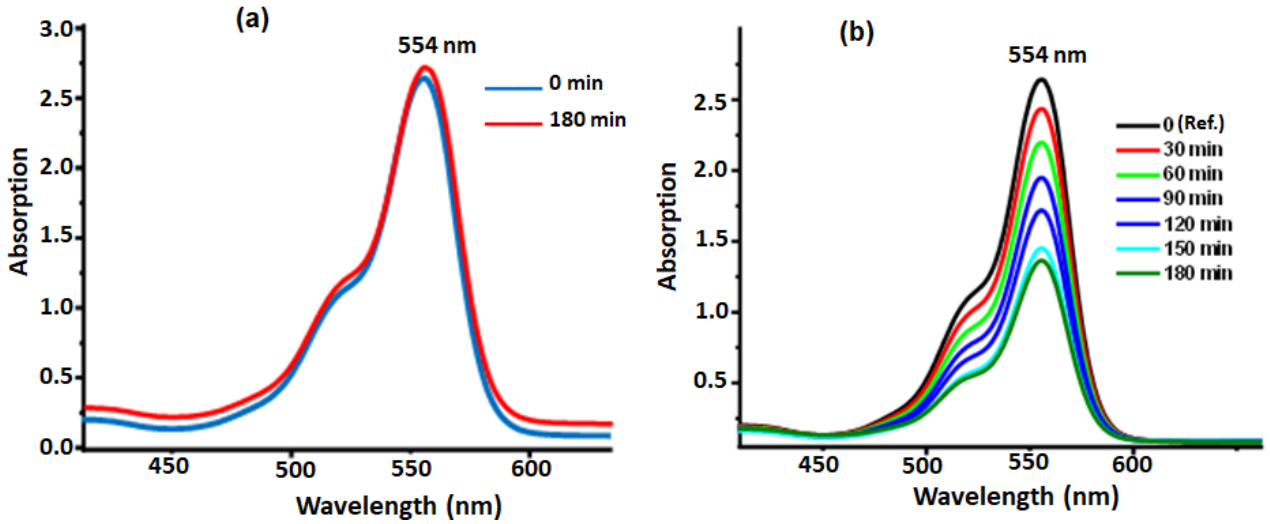

Figure 16. Evolution of the absorbance of RhB over time in H_2O at pH = 7 and 25 °C; **(a):** without catalyst and presence of H_2O_2, **(b):** 10 mg of complex **1**, (at pH = 6, c = 25 mg/L) and H_2O_2 (10 mL/L).

As shown by Figure 16, without the use of complex **1** as catalyst, no degradation of the organic dye occurs even after 180 min of reaction.

As was reported by Nyamunda *et al.,* **[75],** the use of metallic compounds as catalysts in the oxidation of organic species by H_2O_2 is known to involve OH• radicals. The degradation of the RhB dye by the oxidation with a hydrogen peroxide solution in the presence of complex **1** as catalyst can be explained using the following equation 2:

$$\frac{dC}{dt} = -k.C.[OH\cdot] \qquad \textbf{(Eq. 3)}$$

where C is the concentration of RhB dye at time t and k is defined as the second order rate constant of the RhB species with OH•. Given the fact that the concentration of OH• is constant, assuming the steady state situation for the formation rate of these intermediates. The equation can be further simplified if one considers that the concentration of OH• is constant, assuming the steady state situation for the net formation rate of these intermediates. Therefore, the degradation rate of the RhB dye with H_2O_2 in presence of complex **1** is given by Equation 4:

$$\frac{dC}{dt} = -k_o.C \qquad \textbf{(Eq. 4)}$$

where k_o (in min^{-1}) is the pseudo-first order rate constant. The degradation yield [R(%)] of the RhB dye in the above-mentioned conditions is shown in Figure S7 where the C_t/C_o curves are plotted versus time. C_t and C_o are the concentration of RhB at the instants t and t = 0, respectively. The degradation yield (R%) is given by equation 5 as follows:

$$R(\%) = \left(1 - \frac{C_t}{C_o}\right).100 \qquad \textbf{(Eq. 5)}$$

As shown in Figure S7, when we used only the RhB dyes with the aqueous H_2O_2 solution, there was no degradation of the organic dye. The use of the aqueous H_2O_2 solution (C_o = 10 $mg.L^{-1}$) led to a degradation yield of 48.9%, after three hours of reaction. The degradation is best described by a pseudo first-order kinetics with : $Ln\frac{C_t}{C_0} = -ko.t$ **(Eq. 5)** (Figure S7) and the k_o value of the pseudo-first order degradation rate constant regarding the RhB-H_2O_2 complex dye systems is 0.004 min^{-1} (R^2 = 0.9915).

3.9.2. Photodegradation of RhB dye with H_2O_2 using complex 1

The photodegradation reaction of the RhB dye using complex **1** as catalyst was monitored by UV/vis spectroscopy. To follow the photodegradation of RhB we utilized the λ_{max} of the absorption band of the RhB species at ~ 554 nm (in aqueous solution at room temperature). In Figure 17 we report the variation of the λ_{max} of the absorption of the RhB dye upon radiation time, using complex **1** as catalyst. Figure S8-

a shows that the degradation yield of RhB dye in water under light for 180 min at pH = 7 and 25 °C in presence of complex is 73.4% while in absence of light, this degradation is less than 25%

The $Ln\frac{C_t}{C_o}$ versus time plot is depicted in Figure S8. The photodegradation is also described by a pseudo first-order kinetics with : $Ln\frac{C_t}{C_0} = -ko.t$ **(Eq. 6)** (Figure S8-b) where k is the rate constant which was determined to be equal to 0.008 min^{-1} (R^2 = 0.9503).

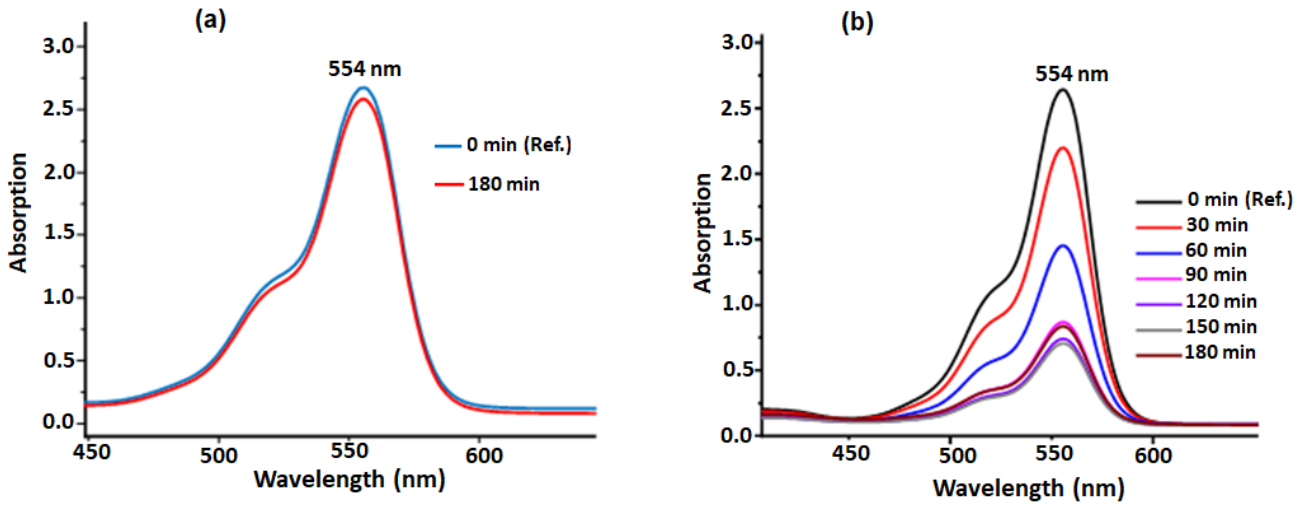

Figure 17. Evolution of the absorbance of the RhB dye over time under visible light in H_2O at pH = 7 and 25 °C. **(a):** without catalyst, **(b):** 10 mg of complex **1**, (at pH = 6, C=25 mg/L) and H_2O_2 (10 mL/L).

The reusability of complex **1** as catalyst in this photodegradation of the rhodamine (RhB) dye was investigated. The catalyst was separated by filtration after each degradation cycle, washed with distilled water and then dried. It was found that the regeneration process could be repeated for four cycles, with efficiencies decreasing from 73.4% to 69.8% after 4 cycles (180 min each).

4. Conclusion

In this work we synthesized and characterized by physicochemical techniques the bis(1,4-diazabicyclo[2.2.2]octane)[*meso*-tetra(*para*-chlorophenyl)porphyrinate]magnesium(II) chloroform disolvate complex with the formula $[Mg(TClPP)(DABCO)_2]\cdot 2CHCl_3$ (**1**). The UV/Vis, fluorescence, ^1H NMR and cyclic voltammetry data are typical for magnesium(II) *meso*-arylporphyrin complexes. The X-ray molecular structure of **1** shows that this porphyrinic species is hexacoordinated and the average equatorial distance Mg-N(pyrrole) is very close to those of the related pentacoordinated and hexacoordinated Mg(II) metalloporphyrins indicating that the nature of the *N*-donor axial ligand don't have important geometric role on this type of porphyrin complexes.

The optimized molecular structure of **1** indicates that the theoretical and experimental distances and angles values are very close. The MEP contour maps of complex **1** show that the Mg(II) center metal and the two DABCO axial ligands exhibit an important electron-accepting properties which is an indication that the DABCO could be easily substituted.

The bis(DABCO) magnesium(II) metalloporphyrin (**1**) was also analyzed by molecular docking methods against two SARS-COV-2 proteins (ACE2 and ORF8) and two oxidase enzymes [Human Peroxidase enzyme (PDB code1HD2) and Peroxiredoxin 5 (PRDX5) (PDB code1H4O)]. This study indicates (i) that the ACE2-MgTClPP(DABCO)$_2$ system possesses the strongest energy score equal to -125.15 kcal/mol and (ii) the " Human Peroxidase-[Mg(TClPP)(DABCO)$_2$]·2CHCl$_3$ " system presents the highest total energy value of -89.68 kcal/mol with an important van der Waals interaction (-89.68 kcal/mol). Furthermore, complex **1** was tested as a catalyst in the degradation of the Rhodamine B dye in presence of a H_2O_2 solution with and in absence of irradiation showing that the photodegradation gives a better yield of 73%.

Supporting information

CCDC-2236148 contain the supplementary crystallographic data of complex **1**. These data can be obtained free of charge from the Cambridge Crystallographic Data Centre via www.ccdc.cam.ac.uk/data_request/cif.

Acknowledgements

The authors gratefully acknowledge financial support from the Ministry of Higher Education and Scientific Research of Tunisia.

4. References

[1] D. Intrieri, C. Damiano, P. Sonzini, E. Gallo, Porphyrin-based homogeneous catalysts for the CO2 cycloaddition to epoxides and aziridines, J. Porphyrins Phthalocyanines 23 (2019) 1–24, doi: 10.1142/S1088424619300015.

[2] B.M.J.M. Suijkerbuijk, D.J. Schamhart, H. Kooijman, A.L. Spek, G. Van Kotena, R.J.M.K. Gebbink, Mono(NCN-pincer palladium)-metalloporphyrincatalysts: evidence for supramolecular bimetallic catalysis, Dalton Trans. 39 (2010) 6198-6216, doi: 10.1039/B925236N.

[3] W. Wang, Y. Wang, C. Li, L. Yan, M. Jiang, Y. Ding, Alternate Biobased Route To Produce δ-Decalactone: Elucidating the Role of Solvent and Hydrogen Evolution in Catalytic Transfer Hydrogenation, ACS Sustain. Chem. Eng. 5 (2017) 4523−4528, doi: 10.1021/acssuschemeng.7b00947.

[4] S. Xie, Y. Chai, Y. Yuan, R. Yuan, Manganese porphyrin–double stranded DNA complex guided in situ deposition of polyaniline for electrochemical thrombin detection, Chem. Commun. 50 (2014) 7169, doi: 10.1039/c4cc02608j.

[5] A. Flórido, N. Saraiva, S. Cerqueira, N. Almeida, M. Parsons, I. Batinic-Haberle, J.P. Miranda, J.G. Costa, G. Carrara, M. Castro, N.G. Oliveira, A.S. Fernandes, The manganese(III) porphyrin MnTnHex-2-PyP5+ modulates intracellular ROS and breast cancer cell migration: Impact on doxorubicin-treated cells, Redox Biology 20 (2019) 367–378, doi: 10.1016/j.redox.2018.10.016.

[6] J. T. Brewster II, G.D. Thiabaud, P. Harvey, H. Zafar, J.F. Reuther, S. Dell'Acqua, R.M. Johnson, H.D. Root, P. Metola, A. Jasanoff, L. Casella, J.L. Sessler, Metallotexaphyrins as MRI-Active Catalytic Antioxidants for Neurodegenerative Disease: A Study on Alzheimer's Disease, Chem, 6, 2020, doi: 10.1016/j.chempr.2019.12.016.

[7] S.R. Alharbi, A.A.A. Darwish, S.E. Al Garni, H.I. ElSaeedy, K.F. Abd El-Rahman, Influence of thickness and annealing on linear and nonlinear optical properties of manganese (III) chloride tetraphenyl porphine (MnTPPCl) organic thin films, Infrared Physics & Technology 78 (2016) 77–83, doi: 10.1016/j.infrared.2016.07.014.

[8] A. Boakye, K. Yu, B.K. Asinyo, H. Chai, T. Raza, T. Xu, G. Zhang, L. Qu, A Portable Electrochemical Sensor Based on Manganese Porphyrin-Functionalized Carbon Cloth for Highly Sensitive Detection of Nitroaromatics and Gaseous Phenol, Langmuir 38 (2022) 12058−12069, doi: 10.1021/acs.langmuir.2c01908.

[9] K. Gkini, N. Balis, M. Papadakis, A. Verykios, M.-C. Skoulikidou, C. Drivas, S. Kennou, M. Golomb, A. Walsh, A.G. Coutsolelos, M. Vasilopoulou, P. Falarasn, Manganese Porphyrin Interface Engineering in Perovskite Solar Cells, ACS Appl. Energy Mater. 3 (2020) 7353−7363, doi: 10.1021/acsaem.0c00710.

[10] A.N. Marianov, Y. Jiang, Effect of Manganese Porphyrin Covalent Immobilization on Electrocatalytic Water Oxidation and Oxygen Reduction Reactions, ACS Sustainable Chem. Eng.7 (2019) 3838−3848, doi: 10.1021/acssuschemeng.8b04735.

[11] T.P. Umile, J.T. Groves, Catalytic Generation of Chlorine Dioxide from Chlorite Using a Water-Soluble Manganese Porphyrin, Angew. Chem. Int. Ed. 50 (2011) 695 –698, doi: 10.1002/anie.201004482.

[12] D. Peng, L. Zhang, R.-P. Liang, J.-D. Qiu, Rapid Detection of Mercury Ions Based on Nitrogen-Doped Graphene Quantum Dots Accelerating Formation of Manganese Porphyrin, ACS Sens. 3 (2018) 1040−1047, doi: 10.1021/acssensors.8b00203.

[13] Y.A. Gubarev, N.Sh. Lebedeva, E.S. Yurina, S.A. Syrbu, A.N. Kiselev, M.A. Lebedev, Possible therapeutic targets and promising drugs based on unsymmetrical hetaryl-substituted porphyrins to combat SARS-CoV-2, J. Pharm. Anal. 11 (2021) 691-698, doi: 10.1016/j.jpha.2021.08.003.

[14] C. Gu, Y. Wu, H. Guo, Y. Zhu, W. Xu, Y. Wang, Y. Zhou, Z. Sun, X. Cai, Y. Li, J. Liu, Z. Huang, Z. Yuan, R. Zhang, Q. Deng, D. Qu, Y. Xie, Protoporphyrin IX and verteporfin prevent SARS-CoV-2 infection in vitro and in a mouse model expressing human ACE2, Sci. Bull. 66 (2021) 925–936, doi: 10.1016/j.scib.2020.12.005.

[15] S. Semiz, Vanadium as potential therapeutic agent for COVID-19: A focus on its antiviral, antiinflamatory, and antihyperglycemic effects, J. Trace Elem. Med. Biol. 69 (2022) 126887, doi: 10.1016/j.jtemb.2021.126887.

[16] A. Almeida, M. Amparo, F. Faustino, M.G.P.M.S. Neves, Antimicrobial Photodynamic Therapy in the Control of COVID-19, Antibiotics 9 (2020) 320, doi:10.3390/antibiotics9060320.

[17] C.R. Groom, I.J. Bruno, M.P. Lightfoot, S.C. Ward, The Cambridge Structural Database, Acta Crystallogr. B Struct. Sci. Cryst. Eng. Mater. 72 (2016) 171–179, doi: 10.1107/S2052520616003954.

[18] K.M. Kadish, M. Morrison, L.A. Constant, Dickens, and D.G. Davis, A study of solvent and substituent effects on the redox potentials and electron-transfer rate constants of substituted iron meso-tetraphenylporphyrins, J. Am. Chem. Soc. 98 (1976) 8387-8390, doi: 10.1021/ja00442a013.

[19] O.C. Choon, V. McKee, G.A. Rodley, Inorg. Chim. Acta 123 (1986) 11, The crystal and molecular structure of a monohydrated dipicoline magnesium tetraphenylporphyrin complex doi: 10.1016/S0020-1693(00)84300-5.

[20] S. Yang, R.A. Jacobson, Synthesis, crystal structure and molecular modeling of aquo magnesium tetra(methoxyphenyl)porphyrin, Inorg. Chim. Acta 190 (1991) 129 doi: 10.1016/S0020-1693(00)80241-8.

[21] N. Amiri, S. Nasri, T. Roisnel, G .Simonneaux, H. Nasri, Crystal structure of di-aqua-[5,10,15,20-tetra-kis-(4-bromo-phen-yl)porphyrinato-[kappa]4N]magnesium, Acta Crystallogr., Sect.E:Cryst.Commun. 71 (2015) m73, doi: 10.1107/S2056989015003722.

[22] S. Jabli, M. Chaabene, T. Roisnel, F. Molton, F. Loiseau, P. Jehan, R. Ben Chaabane, H. Nasri, A combined experimental and theoretical study on the synthesis, spectroscopic characterization of Magnesium(II) porphyrin complex with DMAP axial ligand and antifungal activity, J. Mol. Struct. 1267 (2022) 133559, doi: 10.1016/j.molstruc.2022.133559.

[23] T. Fradi, O. Noureddine, F. Ben Taheur, M. Guergueb, S. Nasri, N. Amiri, A. Almahri, T. Roisnel, V. Guerineau, N. Issoui, H. Nasri, New DMAP meso-arylporphyrin Magnesium(II) complex. Spectroscopic, Cyclic voltammetry and X-ray molecular structure characterization. DFT, DOS and MEP calculations and Antioxidant and Antifungal activities, J. Mol. Struct. 1236 (2021) 130299,

doi: 10.1016/j.molstruc.2021.130299.

[24] R.L. Hill, M. Gouterman, A. Ulman, Tetraphenylporphyrin molecules containing heteroatoms other than nitrogen. 7.1. emission and electronic structure of rings containing sulfur and selenium, Inorg. Chem. 21 (1982) 1450–1455, doi: 10.1021/ic00134a037.

[25] E.J. Shin, D. Kim, Substituent effect on the fluorescence quenching of various tetraphenylporphyrins by ruthenium tris(2,2'-bipyridine) complex, J. Photochem. Photobiol. A 152 (2002) 25–31, doi: 10.1016/S1010- 6030(02)00189- 2.

[26] A.D. Adler, F.R. Longo, J.D. Finarelli, J. Goldmacher, J. Assour, L. Korsakoff, A simplified synthesis for meso-tetraphenylporphine, J. Org. Chem. 32 (1967) 476, doi: 10.1021/jo01288a053.

[27] A. Ghosh, S.M. Mobin, R. Fröhlich, R.J. Butcher, D.K. Maity, M. Ravikanth, Effect of Five Membered Versus Six Membered Meso-Substituents on Structure and Electronic Properties of Mg(II) Porphyrins: A Combined Experimental and Theoretical Study, Inorg. Chem. 49 (2010) 8287–8297, doi: 10.1021/ic1008522.

[28] M.J. Frisch, et al., GAUSSIAN 09, Revision A.02, Gaussian, Inc., Wallingford, CT, 2009.

[29] GaussView, Guassian, Inc. (Carnergie Office Parck-Building6 Pittsburgh PA 151064 USAR), Copyright © 2000-2003 Semichem. Inc..

[30] Bruker (2004). SAINT, APEX2 and SADABS. Bruker AXS Inc., Madison, Wisconsin, USA.

[31] M.C. Burla, R. Caliandro, B. Carrozzini, G.L. Cascarano, C. Cuocci, C. Giacovazzo, M. Mallamo, A. Mazzone, G. Polidori, Crystal structure determination and refinement via SIR2014, J. Appl. Cryst. 48 (2015). 306–309, doi: 10.1107/S1600576715001132.

[32] G.M. Sheldrick, SHELXT - Integrated space-group and crystal-structure determination Acta Cryst , C71 (2015) 3-8, doi: 10.1107/S2053273314026370.
[33] P. McArdle, SORTX - a program for on-screen stick-model editing and autosorting of SHELX files for use on a PC, J. Appl. Crystallogr. 28 (1995) 65, doi:.org/10.1107/S0021889894010642.

[34] A.L. Spek, PLATON, An Integrated Tool for the Analysis of the Results of a Single Crystal Structure Determination, Acta Cryst A. 46 (1990) 34–34. doi: 10.1107/S0108767390099780.

[35] C.F. Macrae, I.J. Bruno, J.A. Chisholm, P.R. Edgington, P. McCabe, E. Pidcock, L. Rodriguez-Monge, R. Taylor, J. van de Streek, P.A. Wood, Mercury CSD 2.0 – new features for the visualization and investigation of crystal structures, J Appl Crystallogr. 41 (2008) 466–470. doi: 10.1107/S0021889807067908.

[36] N. Amiri, M. Hajji, F. Ben Taheur, S. Chevreux, T. Roisnel, G. Lemercier, H. Nasri, Two novel magnesium(II) meso-tetraphenylporphyrin-based coordination complexes: Syntheses, combined

experimental and theoretical structures elucidation, spectroscopy, photophysical properties and antibacterial activity, J. Solid State Chem. (2018), 258, 477, doi: 10.1016/j.jssc.2017.11.018.

[37] N. Amiri, M. Bourguiba, M. Guergueb, S. Chevreux, H. Nasri, Synthesis, molecular structure, spectroscopic characterization and dielectric properties of new cobalt(II) meso-tetraphenylporphyrin-based coordination complex, Inorg. Chem. Commun.118 (2020) 107995, doi: 10.1016/j.inoche.2020.107995.

[38] S. Jabli, S. Hrichi, R. Chaabane-Banaoues, F. Molton, F. Loiseau, T. Roisnel, I. Turowska-Tyrk, H. Babba, H. Nasri, Study on the synthesis, physicochemical, electrochemical properties, molecular structure and antifungal activities of the 4-pyrrolidinopyridine Mg(II) meso-tetratolylporphyrin complex, J. Mol. Struct. 1261 (2022) 132882, doi: 10.1016/j.molstruc.2022.132882.

[39] K. Colladet, M. Nicolas, L. Goris, L. Lutsen, D. Vanderzande, Low-band gap polymers for photovoltaic applications, Thin Solid Films 451 (2004) 7–11, doi: 10.1016/j.tsf.2003.10.085.

[40] C.C. Mak, N. Bampos and J.K.M. Sanders, Metalloporphyrin Dendrimers with Folding Arms, Angew. Chem., Int. Ed., 1998, 37, 3020–3023, doi: 10.1002/(SICI)1521-3773(19981116)37:21%3C3020::AID-ANIE3020%3E3.0.CO;2-S

[41] J. Zhang, P. Zhang, Z. Zhang, X. Wei, Spectroscopic and Kinetic Studies of Photochemical Reaction of Magnesium Tetraphenylporphyrin with Oxygen, J. Phys. Chem. A 113 (2009) 5367–5374, doi: 10.1021/jp811209k.

[42] K. Ezzayani, A. Ben Khelifa, E. Saint-Aman, F. Loiseau, H. Nasri, Synthesis, spectroscopic characterizations, cyclic voltammetry investigation and molecular structure of the di-μ-cyanato-N-bis(μ-1,4,7,10,13,16-hexaoxacyclooctadecane)bis(5,10,15,20tetraphenylporphyrinato)dimagnesium dipotassium complex, Polyhedron 117 (2016) 817-825, doi: 10.1016/j.poly.2016.06.045.

[43] M. Guergueb, S. Nasri, J. Brahmi, F. Loiseau, F. Molton, T. Roisnel, V. Guerineau, I. Turowska-Tyrk, K. Aouadi, H. Nasri, Effect of the coordination of π-acceptor 4-cyanopyridine ligand on the structural and electronic properties of meso-tetra(para-methoxy) and meso-tetra(para-chlorophenyl) porphyrin cobalt(II) coordination compounds. Application in the catalytic degradation of methylene blue dye, RSC Adv., 2020, 10, 6900, doi: 10.1039/c9ra08504a.

[44] N. Amiri, F. Ben Taheur, S. Chevreux, E. Wenger, G. Lemercier, H. Nasri, Synthesis, crystal structure and spectroscopic characterizations of porphyrin-based Mg(II) complexes – Potential application as antibacterial agent, Tetrahedron 73 (2017) 7011e7016, doi : 10.1016/j.tet.2017.10.029

[45] K. Ezzayani, Z. Denden, E. Saint-Aman, S. Najmudin, F. Loiseau, H. Nasri, Exploring the Effects of Axial Pseudohalide Ligands on the Photophysical and Cyclic Voltammetry Properties and Molecular Structures of MgII Tetraphenyl/porphyrin Complexes, Eur J. Inorg. Chem. (2014) 5348, doi: 10.1002/ejic.201402546.

[46] K. Ezzayani, A. Ben Khelifa, F. Ben Taheur, M. Guergueb, A. Mansour, J.-C. Daran, H. Nasri, Building-up novel coordination polymer with magnesium porphyrin: Synthesis, molecular structure, photophysical properties and spectroscopic characterization. Potential application as antibacterial agent, Inorganica Chim. Acta 514 (2021) 119960, doi: 10.1016/j.ica.2020.119960.

[47] N. Amiri, M. Hajji, T. Roisnel, G. Simonneaux, H. Nasri, Synthesis, molecular structure, photophysical properties and spectroscopic characterization of new 1D-magnesium(II) porphyrin-based coordination polymer, Res Chem Intermed 44 (2018) 5583–5595, doi: 10.1007/s11164- 018- 3442-9.

[48] A. Ghosh, S.M. Mobin, R. Frohlich, R.J. Butcher, D.K. Maity, M. Ravikanth, Effect of Five Membered Versus Six Membered Meso-Substituents on Structure and Electronic Properties of Mg(II) Porphyrins: A Combined Experimental and Theoretical Study, Inorg. Chem. 49 (2010) 8287-8297, doi: 10.1021/ic1008522.

[49] K. Ezzayani, A. B. Khelifa, E. Saint-Aman, F. Loiseau, H. Nasri, Complex of hexamethylenetetramine with magnesium-tetraphenylporphyrin: Synthesis, structure, spectroscopic characterizations and electrochemical properties, J. Mol. Struct., 1137 (2017) 412-418, doi: 10.1016/j.molstruc.2017.02.054.

[50] C.G. Oliveri, J. Heo, S.T. Nguyen, C.A. Mirkin, Z. Wawrzak, A Convergent Coordination Chemistry-Based Approach to Dissymmetric Macrocyclic Cofacial Porphyrin Complexes, Inorg. Chem. 46 (2007) 7716, doi:.org/10.1021/ic701424j.

[51] J. Bhuyan, R. Sarkar, S. Sarkar, A Magnesium Porphyrin Bicarbonate Complex with CO2-Modulated Photosystem I Action, Angew. Chem., Int. Ed. 50 (2011) 50 10603, doi: 10.1002/anie.201103876.

[52] V. McKee, C. C. Ong, G. A. Rodley, X-ray crystal and molecular structures of related octahedral magnesium tetraphenylporphyrin complexes, Inorg.Chem. 23 (1984) 4242, doi: 10.1021/ic00193a029.

[53] M.P. Byrn, C.J. Curtis, Y. Hsiou, S.I. Khan, P.A. Sawin, S.K. Tendick, A. Terzis, C.E. Strouse, Porphyrin sponges: conservative of host structure in over 200 porphyrin-based lattice clathrates, J. Am. Chem. Soc. 115 (1993), 115, 9480, doi: 10.1021/ja00074a013.

[54] R.I. Yousef, B. Walfort, T. Ruffer, C. Wagner, H. Schmidt, R. Herzog, D. Steinborn, R.I. Yousef, B. Walfort, T. Ruffer, C. Wagner, H. Schmidt, R. Herzog, D. Steinborn, doi: 10.1016/j.jorganchem.2004.10.058.

[55] S. Harder, M. Wiesinger, B. Maitland, H. Elsen, J. Pahl, Stabilizing Magnesium Hydride Complexes with Neutral Ligands, Eur. J. Inorg. Chem. (2019) 4433, doi: 10.1002/ejic.201900936.

[56] M.J. Turner, J.J. McKinnon, S.K. Wolff, D.J. Grimwood, P.R. Spackman, D. Jayatilaka, M.A. Spackman, CrystalExplorer17; The University of Western Australia : Perth, Australia, 2017.

[57] O. Noureddine, S. Gatfaoui, S. A. Brandan, H. Marouani, N. Issaoui. Structural, docking and spectroscopic studies of a new piperazine derivative, 1-phenylpiperazine-1,4-diium-bis (hydrogen sulfate), J. Mol. Struct. 1202 (2020) 127351, doi: 10.1016/j.molstruc.2019.127351.

[58] O. Noureddine, S. Gatfaoui, S. A. Brandan, A. Saagama, H. Marouani, N. Issaoui, Experimental and DFT studies on the molecular structure, spectroscopic properties, and molecular docking of 4-phenylpiperazine-1-ium dihydrogen phosphate, J. Mol. Struct. 1207 (2020) 127762, doi: 10.1016/j.molstruc.2020.127762.

[59] O. Noureddine, N. Issaoui, S. Gatfaoui, O. Al-dossary, H. Marouani, Quantum chemical calculations, spectroscopic properties and molecular docking studies of a novel piperazine derivative, J. King Saud Univ. Sci. 33 (2021) 101283, doi: 10.1016/j.jksus.2020.101283.

[60] N. Issaoui, H. Ghalla, F. Bardak, M. Karabacak, N. A. Dlala, H. T. Flakus, B. Oujia, Combined experimental and theoretical studies on the molecular structures, spectroscopy, and inhibitor activity of 3-(2-thienyl) acrylic acid through AIM, NBO, FT-IR, FT-Raman, UV and HOMO-LUMO analyses, and molecular docking. J. Mol. Struct. 1130 (2017) 659., doi: 10.1016/j.molstruc.2016.11.019.

[61] K.-C. Hsu, Y.-F. Chen, S.-R. Lin, J.-M. Yang, iGEMDOCK: a graphical environment of enhancing GEMDOCK using pharmacological interactions and post-screening analysis, BMC Bioinformatics 12 (Suppl 1), S33 (2011), doi: 10.1186/1471-2105-12-S1-S33

[62] O.S. Smart, V. Horský, S. Gore, R.S. Vařeková, V. Bendová, G.J. Kleywegt, S. Velankar, Structural Biology, 74 (2018) 237-244, doi: 10.1107/S2059798318003303.

[63] D.S. Visualizer, Accelrys software inc. Discovery Studio Visualizer 2, 2005.

[64] U. Singh, A.M. Malla, I.A. Bhat, A. Ahm, M.N. Bukhari, S. Bhat, S. Anayutullah, A.A. Hashmi, Synthesis, molecular docking and evaluation of antifungal activity of Ni(II),Co(II) and Cu(II) complexes of porphyrin core macromolecular ligand, Microbial pathogenesis 93 (2016) 172-179, doi: 10.1016/j.micpath.2016.02.011.

[65] G.S. Masaret, Synthesis, biological evaluation, and docking studies of various substituted porphyrin conjugates embedded with N-containing heterocycles, J. Heterocycl. Chem. 58 (2021) 1836-1848, doi: 10.1002/jhet.4314.

[66] T. Ali, N. Muhammad, Za. Ali, A. Samad, M. Ibrahim, M. Ikram, S Rehman, S. Shujah, G. S. Khan, A. Wadood, S. Ali, C. Schulzke, J. Mol. Struct. 1234 (2021) 130190, https://doi.org/10.1016/j.molstruc.2021.130190

[67] M. Saeed, M. Muneer, A. ul Haq, N. Akram, Environ. Sci. Pollut. Res. 29 (2022) 293–311, doi: 10.1007/s11356-021-16389-7.

[68] S. Khan, I. Khan, M. Sadiq, N. Muhammad, Inorg. Chem. Commun. 150 (2023) 110556, doi: 10.1016/j.inoche.2023.110556.

[69] S. Khan, A. Noor, I. Khan, M. Muhammad, M. Sadiq, N Muhammad, Catalysts 13 2023 44. doi: 10.3390/catal13010044.

[70] S. Khan, M. Sadiq, D. -S. Kim, M. Ullah, N. Muhammad, Appl. Water Sci. 12 (2022) 118, doi: 10.1007/s13201-022-01628-0.

[71] O. Üner, Ü. Geçgel, H. Kolancilar, Y. Bayrak, Chem. Eng. Commun., 204 (2017) 772–783, doi: 10.1080/00986445.2017.1319361.

[72] : X. Gao, Y. Zhang, Y. Dai and F. Fu, J. Solid State Chem., 239 (2016) 265–273, doi: 10.1016/j.jssc.2016.05.001.

[73] T. L. Yusuf, B. O. Orimolade, D. Masekela, B. Mamba, N. Mabuba, RSC Adv. 12 (2022) 26176-26191, doi: 10.1039/D2RA04236C.

[74] C. Wang, P. Shi, C. Guo, R. Guo, J. Qiu, J. Electroanal. Chem. 956 (2024) 118072, doi: 10.1016/j.jelechem.2024.118072.

[75] B.C. Nyamunda, F. Chigondo, Hydrogen peroxide as an oxidant for organic reactions, J. Atoms Mol. 3 (2013) 23–44.